Project acronym:	Lasers4MaaS
Project title:	Laser-as-a-Service Digital Platform with Dynamic Beam Shaping for Acceleration of Smart, Decentralised and Sustainable Factory of the Future
Call	HORIZON-CL4-2024-TWIN-TRANSITION-01-03 Manufacturing-as-Service: technologies for customised, flexible, and decentralised production on demand
Grant agreement No:	101178719
Work-package 11:	IIoT sensors selection and generation of weld data configurations
Deliverable D11.1:	IIoT sensors selection and characterisation
Owner:	WMG
Due date:	31//05/2026

Type		
R	Document, report (excluding the periodic and final reports)	x
DEM	Demonstrator, pilot, prototype, plan designs	
DEC	Websites, patents filling, press & media actions, videos, etc	
DATA	Data sets, microdata, etc	
DMP	Data management plan	
ETHICS	Deliverables related to ethics issues	
SECURITY	Deliverable related to security issues	
OTHER	Software, technical diagram, algorithms, models, etc	

Dissemination level		
PU	Public, fully open, e.g. project website	x
SEN	Sensitive, limited under the conditions of the Grant Agreement	
Classified R-UE/EU-R	EU RESTRICTED under the Commission Decision No2015/444	

Disclaimers: this project has received funding from the European Union's HORIZON EUROPE research and innovation programme under grant agreement No. 101178719. The content of this publication is the sole responsibility of the Consortium partners listed herein and does not necessarily represent the view of the European Commission or its services.

HISTORY OF CHANGES

Version	Publication date	Change
1.1	07/05/2026	First draft
2.0	08/05/2026	Second draft with all sensors described
3.0	14/05/2026	Third draft with summary and exploitation
4.0	20/05/2026	Final version

LIST OF AUTHORS

Name	Organization	Email
Pasquale Franciosa	WMG	p.franciosa@warwick.ac.uk
Sharhid Jabar	WMG	sharhid.jabar@warwick.ac.uk
Sattar Ghasemi	WMG	sattar.ghasemi@warwick.ac.uk
Tobias Hohmann	FFT	tobias.hohmann@fft.de
Denis Washington	FUTURICE	denis.washington@futurice.com
Christoph Nützel	FUTURICE	christoph.nuetzel@futurice.com
Haim Touitou	CIVAN	haim.touitou@civanlasers.com
Linda Eller-Shein	CIVAN	linda.shein@civanlasers.com
Tjorben Griemsmann	CIVAN	Tjorben.Griemsmann@civanlasers.com
Laszlo Vörös	TUW	laszlo.voeroes@tuwien.ac.at

REVIEWED BY

Name	Organization	Email
Pasquale Franciosa	WMG	p.franciosa@warwick.ac.uk

TABLE OF CONTENTS

1. Executive summary **6**
2. Project requirements **6**
3. Overall system configurations **7**
3.1. WMG setup **7**
3.2. FFT/ECOR setup **7**
4. T11.1. Selection of sensors for product, process and machine monitoring **9**
4.1. Product and process-related sensors **9**
4.1.1. In-process sensors: co-axial camera and process camera **9**
4.1.2. In-process sensors: photodiodes **10**
4.1.3. In-process sensors: optical microphone **10**
4.1.4. In-process sensors: optical coherent tomography **11**
4.2. Machine-related sensors **12**
4.2.1. Machine monitoring sensors: beam shape camera **12**
4.2.2. Machine monitoring sensors: laser analogue power **13**
4.2.3. Machine monitoring sensors: flow meters **13**
4.2.4. Machine monitoring sensors: energy meters **14**
5. T11.2 Testing of sensors and characterisation of KPIs, integration and data acquisition system **15**
5.1. Data policy and data synchronisation **15**
5.2. Data acquisition systems **16**
5.3. Characterization of sensors **17**
5.4. Testing of sensors **19**
6. T11.3 Feature extraction, data labelling, data fusion and augmentation and storage in the database **25**
6.1. Feature extraction, data processing and labelling **25**
6.2. Data fusion and augmentation **25**
6.3. Integration with the Lasers4MaaS platform and storage into the database **27**
7. Summary observations **29**
8. Contribution to project KPIs and expected outcomes **30**
9. Impact and exploitation potentials **30**

LIST OF FIGURES

Figure 1: System configurations at FFT/ECOR (left) and WMG (right). 6
Figure 2: Data acquisition flow from local sensors to the Lasers4MaaS platform. 7
Figure 3: Integration configurations at WMG (red show control signals, dark teal sensor signals) 8
Figure 4: Integration configurations at FFT/ECOR 8
Figure 5: Co-axial camera and photodiode interface. 9
Figure 6: Installation of co-axial camera with integrated beam splitter (WMG setup). 9
Figure 7: Configuration with the optical microphone. 10
Figure 8: OCT source wavelength 11
Figure 9: Mechanical design (left) and physical integration (right) of the OCT system 12
Figure 10: Left - nominal shape. Right - beam shape collected by the beam shape camera 12
Figure 11: The laser analogue power monitoring system 13
Figure 12: Pneumatical energy consumption system 14
Figure 13: Energy meter systems integrated in the master PLC board 14
Figure 14: Data policy and data synchronization overview 15
Figure 15: Data acquisition system - production intent 17
Figure 16: Data processing pipeline of the selected sensors. 18
Figure 17: Influence of airblade position on plume formation and resulting weld depth. 20
Figure 18: Plume intensity analysis. 21
Figure 19: Results of photodiode sensing. 22
Figure 20: Acoustic emission spectra measured with the optical microphone. 23
Figure 21: Values derived from the optical microphone's frequency analysis. 24
Figure 22: Example of feature extraction (left: video with velocity field; right: velocity map) 25
Figure 23: VTK data of a simulated moving laser beam from Comsol (left) to MATLAB (right) 26
Figure 24: FOM vs ROM (left); interpolation of sensor data to the FOM and ROM models (right) 26
Figure 25: Data flow to the Lasers4MaaS platform 28

LIST OF TABLES

Table 1: Sensor data, data format and processing flow.....7
Table 2: Summary of sensors for product and process monitoring.....29

LIST OF ABBREVIATIONS

CFD	Computational Fluid Dynamics
DAQ	Data Acquisition Card
DBS	Dynamic Beam Shaping
FOM	Full Order Model
IIoT	Industrial Internet-of-Things
KPIs	Key Performance Indicators
LWM	Laser Welding Monitoring
LWO	Laser Welding Operation
OCT	Optical Coherent Tomography
ROM	Reduced Order Model
VTK	Visualization Toolkit
WP	Work-package

1. Executive summary

This deliverable summarises the findings related to WP11 (IIoT sensors selection and generation of weld data configurations) and discuss the results related to the following tasks:
(1) **T11.1 Selection of sensors for product, process, machine monitoring** - selection of IIoT sensors for product and process monitoring (e.g., photodiodes, high speed camera, optical coherent tomography, acoustic emissions) and machine monitoring (e.g., flow rates, laser power, beam shape images).
(2) **T11.2 Testing of sensors and characterisation of KPIs, integration of data acquisition system**. Sensor characterisation to perform identification and classification of the KPIs and ultimately support the inspection-diagnosis-correction-prediction quality loop, along with data acquisition systems.
(3) **T11.3 Feature extraction, data labelling, data fusion and augmentation and storage in database**. Data processing, data fusion, data augmentation with synthetic from simulation models.

2. Project requirements

Selection of sensors and technologies for data processing have been driven by the following requirements:

- **Interoperability**: enable connectivity via well-defined interfaces and data formats, building on established industry standards where possible and sensible, to ease data exchange and integration into the wider digital landscape.

- **Integration**: The sensing and monitoring solutions must be compatible with existing mechanical, electrical and optical system architectures. This includes physical integration within constrained manufacturing environments, compatibility with existing laser processing equipment, and minimal disruption to current production workflows. Particular attention has been given to ensuring that sensors and auxiliary systems can be integrated with existing machine components, beam delivery systems, optics, and automation infrastructure.

- **Measurability**: The selected sensing technologies must provide the capability to directly or indirectly measure parameters relevant to the project KPIs and manufacturing objectives. This includes acquisition of process, machine, and quality-related variables required for process monitoring, predictive maintenance, adaptive control, energy assessment, and weld quality evaluation. The sensing infrastructure therefore supports both real-time operational monitoring and higher-level analytics required for intelligent manufacturing applications.

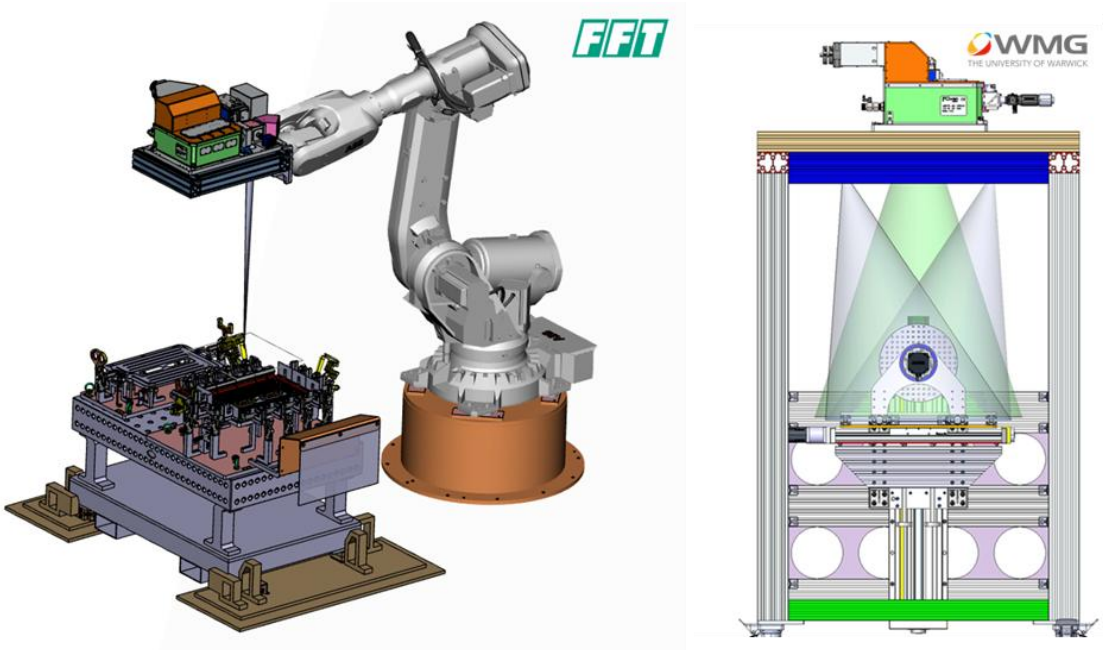

Figure 1: System configurations at FFT/ECOR (left) and WMG (right).

3. Overall system configurations

We have developed two demonstration areas (FFT/ECOR and WMG) to help supporting the testing of the Lasers4MaaS platform across decentralised facilities. The FFT/ECOR setup makes use of a 6-axis robot, while the WMG facility integrates the DBS laser on a stationary frame (Figure 1).

The data acquisition flow is based on "acquire-analyze-transmit-post" logic, as show in Figure 2.

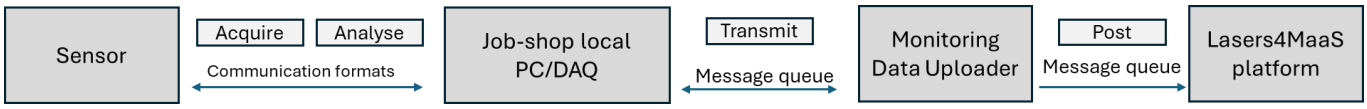

Figure 2: Data acquisition flow from local sensors to the Lasers4MaaS platform.

Both facilities are equipped with various sensors, as listed in Table 1. The sensor readings are acquired and pre-processed on a computer located on the shop floor. An application running on that same computer regularly transfers the latest pre-processed data to the Lasers4MaaS platform in the cloud (see section 4.6 for details).

Table 1: Sensor data, data format and processing flow

Sensor/source	Communication	Data processing	Data type	Data frequency	Output frequency
Gas flow meter	IO-Link/ProfiNET/ Analogue	Filtering, feature extraction	time series	ms	s/min
Energy meter	ProfNet/Analogue	Filtering, feature extraction	time series	ms	s/min
Scanner laser output (input to the laser)	Analogue	Filtering, feature extraction	time series	every weld	every weld
Laser source output (output to workpiece)	Analogue	Filtering, feature extraction	time series	every weld	every weld
Photodiode	Analogue	Filtering, feature extraction	time series	ms	every weld
Beam alignment co-axial camera	USB3/GigeE	ROI cropping, seam detection	images	ms	every weld
Beam shape co-axial camera	API	Beam shape detection	images	every weld	every weld

3.1. WMG setup

The system configuration is shown in Figure 3. The master PC does communicate to the individual devices as follows (more details in D4.1):

- Master PC to SmartMove scanner: TCP-IP communication. SmartMove scanner is the master for the CIVAN OPA6 14 kW
- Master PC to 3-axis welding table: OPC-UA. The 3-axis of the welding table move in sync but independently from the SmartMove scanner
- Master PC to co-axial camera with illumination: USB3. The camera is controlled by the master PC which then, via a dedicated PLC board sync with the LED illumination

The DAQ PC is connected to the sensors via a DAQ NI module, reading sensors data, processing them, and ready for streaming to the FUTURICE application.

3.2. FFT/ECOR setup

The system configuration of FFT/ECOR shopfloor is shown in Figure 4. The master PC/workstation overtakes the overall system orchestration, communicates to the individual devices and is used for centralized data management at shopfloor level:

- SIMATIC Workstation system orchestration: ProfiSAFE communication between general laser booth safety equipment as well as individual technology equipment (HIP, Fixtures, laser, robot, chiller, etc.). ProfiNET communication for the individual control of each system component to

ensure synchronised operation between individual system elements

- Power supply cabinet: Individual power supply and fuse for all system components, as well as usage of switches and routers for centralised system communication. Integrated energy consumption sensor at main switch. Router for access to Lasers4MaaS Platform via FFT Isolation Network.
- Hall Installation Plate (HIP): Treatment of compressed air supply, Spau sensor for air consumption detection
- ABB IRC 5 robot: Communication via digital and analogue output, serial and http commands.
- Technology PC for sensor data collection of CIVAN laser system.

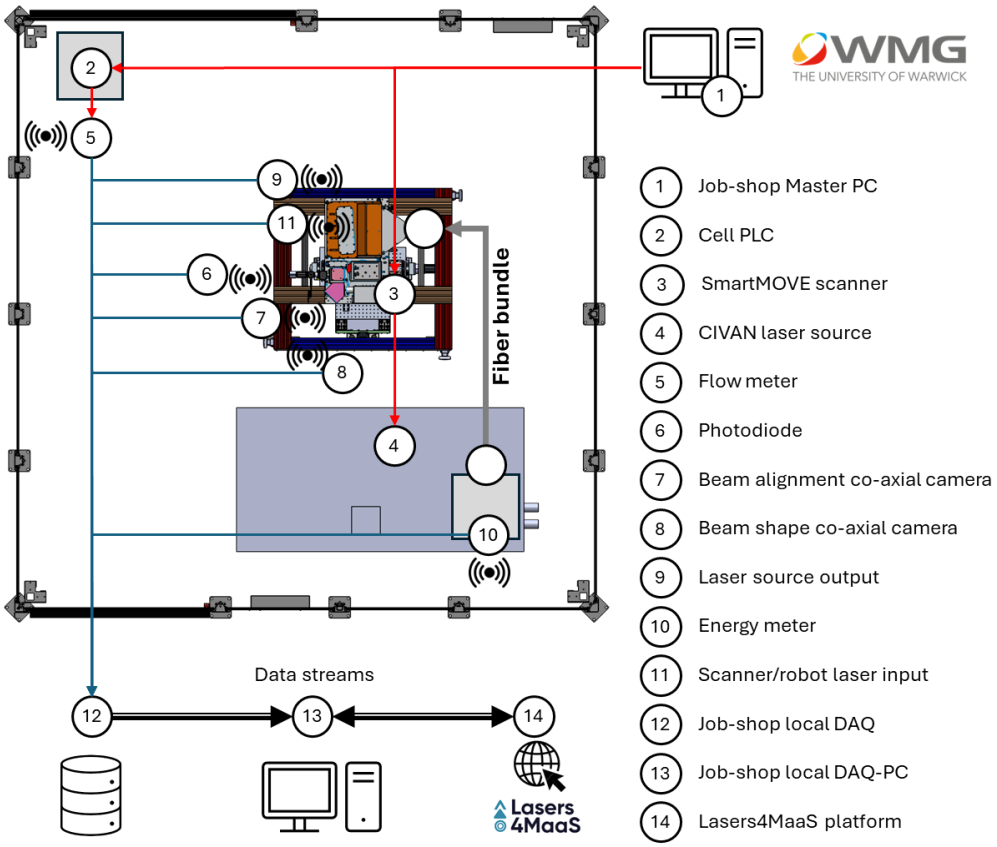

Figure 3: Integration configurations at WMG (red show control signals, dark teal sensor signals)

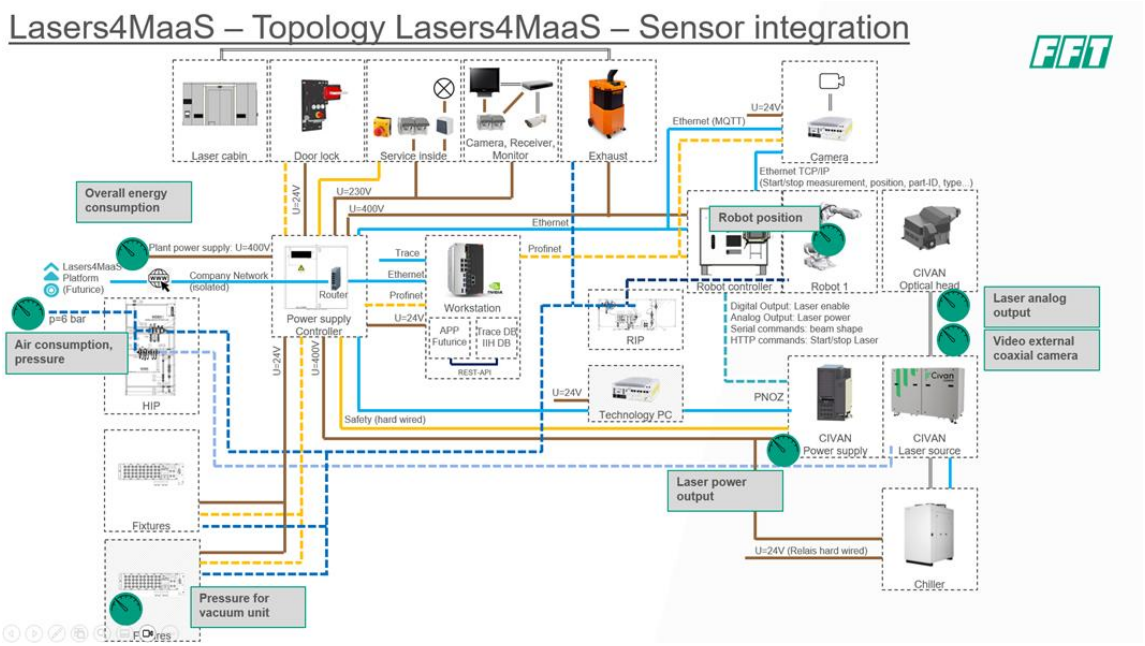

Figure 4: Integration configurations at FFT/ECOR

4. T11.1. Selection of sensors for product, process and machine monitoring

4.1. Product and process-related sensors

4.1.1. In-process sensors: co-axial camera and process camera

The adopted co-axial camera is the Image Source DMK 33UX287, which incorporates a Sony IMX287 CMOS sensor for monochrome image acquisition. The camera provides a resolution of 720 × 540 pixels with a pixel size of 6.9 µm × 6.9 µm and operates using a global shutter architecture. It supports high-speed imaging with frame rates of up to 525 fps and communicates through a USB 3.1 interface. The camera is designed for industrial machine-vision applications and is compatible with standard machine-vision SDK environments, but also MATLAB. A band-pass filter (620 nm (Thorlabs - FBH620-10) and 850 nm (Thorlabs FBH850-40)) has been also integrated in the optical path for spectral filtering.

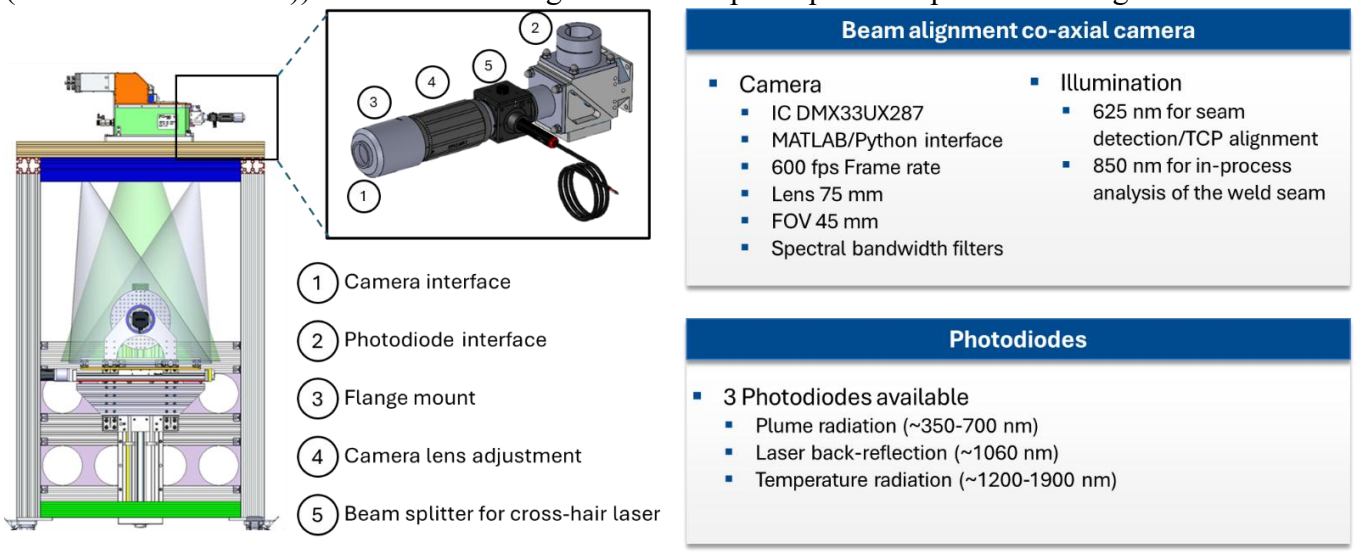

Figure 5: Co-axial camera and photodiode interface.

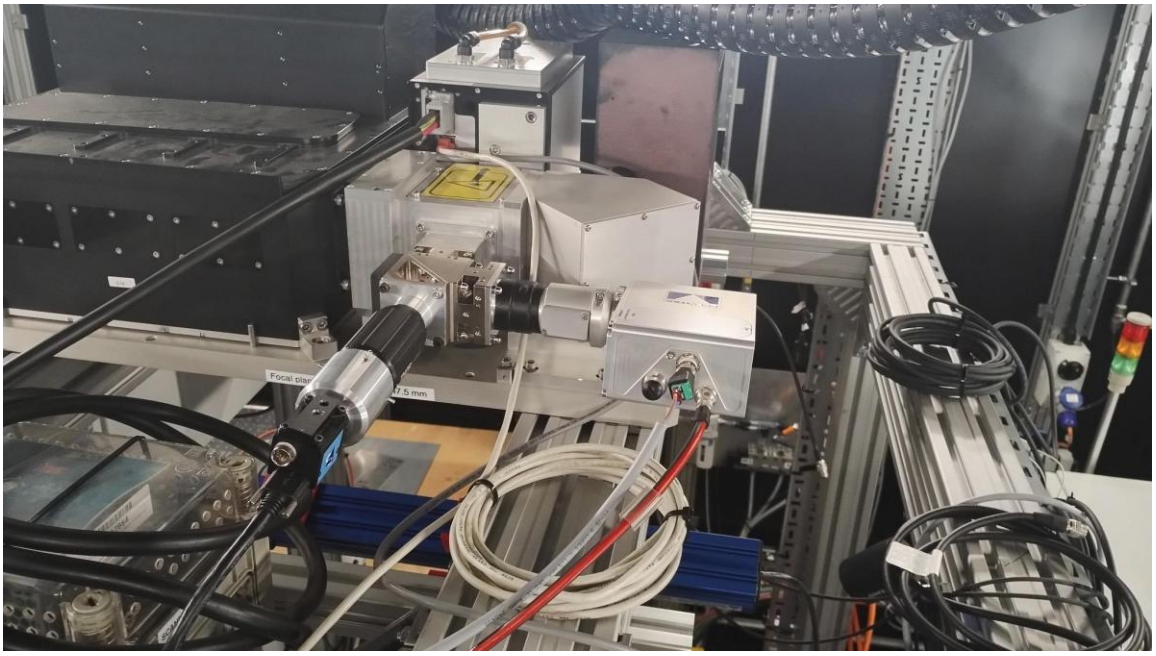

Figure 6: Installation of co-axial camera with integrated beam splitter (WMG setup).

The welding area is flood lit by dedicated LEV lighting system which covers the full FOV (field of view) of the laser beam optics. The lighting comprises of 2 static rows of LED light bars which fills the FOV with 2 selected wavelengths: (1) before welding – 625 nm for seam detection/alignment purpose; (2) during

welding (in-process) – 850 nm for in-process analysis of the weld seam. LEDs are sync to the co-axial camera: the pin 10 (STROBE_OUT) to a positive voltage through a pull-up resistor and then to the pin 4 (bleck wire) of both the illuminators. Then LED is powered through pin 1 (24V) and 3 (GND). In this way the camera can generate a trigger and acquire an image and at the same time give the start signal to both the LEDs. The co-axial camera is mounted on dedicated beam splitter that serves the photodiode too. An adjustable focus unit allows to precisely set the focus of the camera.

Extensive testing was conducted to optimise the exposure and iris aperture settings. The blue LED configuration was found to be compatible with both the scanner system and the LWM/photodiode sensor, while also providing good contrast against the colder background regions. However, image saturation at the laser hot spot was still observed. The red LED configuration (850 nm) also produced good contrast with the colder background, but it was not compatible with the arrangement of the LWM sensor (see next section – the transmission window for the visible radiation is ~350-700 nm).

Only for the process development and optimisation, a high-speed camera (FASTCAM Nova S6 – Photron, Japan) is used to capture the dynamic behaviour and intensity of the plume. The FASTCAM Nova S6 incorporates a CMOS sensor with a full-frame resolution of 1024 × 1024 pixels and supports image acquisition at up to 6.4k fps at full resolution. By reducing the acquisition window, frame rates up to 800k fps can be achieved, enabling the observation of extremely rapid transient phenomena.

4.1.2. In-process sensors: photodiodes

The sensor used was the LWM from Precitec. Details of the mechanical setup are provided in the previous section in Figure 5/6. In the setup the laser beam is pre-focused and the LWM is mounted after the focusing lens of the DBS laser. At the outlet port of the DBS optical head, a beam splitter (YW30-Precitec) has been inserted with the following reflection/transmission properties: UV and visible light: 50/50; IR: 80/20; laser back-reflection: 80/20. A focusing lens (40 mm) is placed at the sensor inlet to localise the intensity of the optical emission before it does reach the sensor itself. The system integrates three sets of photodiodes which detect optical emissions: UV and visible radiation (~350-700 nm); laser back-reflection (~1060 nm); IR radiation (~1200-1900 nm). The signals are coded as analogue outputs in the range of 0-10 V and recorded at the maximum sampling rate of 50 kHz.

4.1.3. In-process sensors: optical microphone

An off-axis optical microphone (Eta 250 ultra - Xarion, Austria) has been also tested, and placed 45 mm above the weld zone (Z-direction) and 10 mm laterally from the beam path (Y-direction), having the sensing face oriented perpendicular to the laser-material interaction area. To synchronize the acoustic signal with the laser welding process, an MSO3014 oscilloscope (Tektronix, Oregon) was employed with a sampling frequency of 2.5 MHz, resulting in a total of 5 million data points collected.

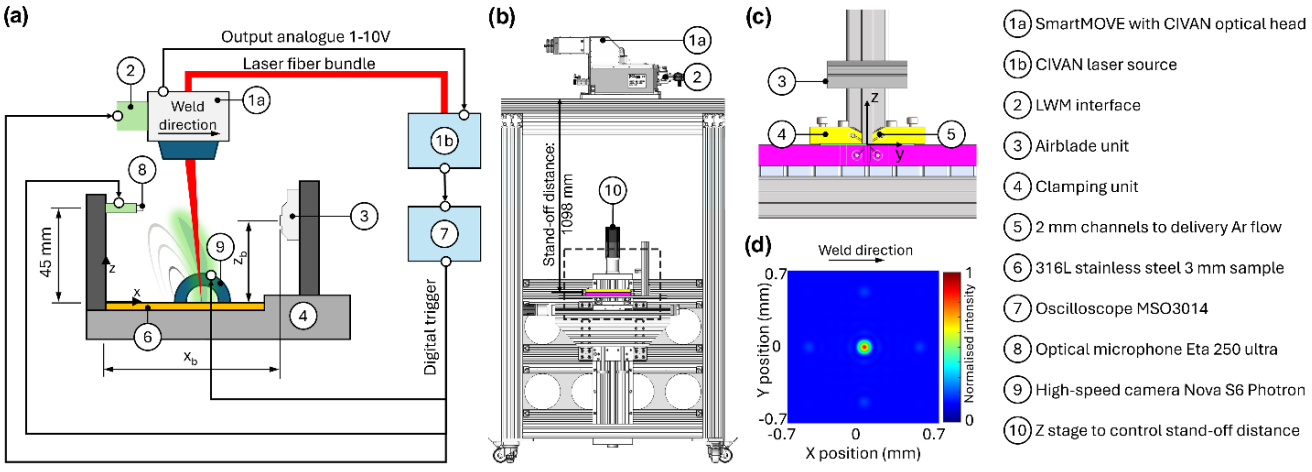

Figure 7: Configuration with the optical microphone.

4.1.4. In-process sensors: optical coherent tomography

OCT was tested independently without the beam splitter used for the LWM. This is to avoid any additional optical filtering. Five precision optical windows/discs made from Corning 7980 fused silica were purchased. The components were manufactured with a diameter of approximately 75 mm and thickness of ~12.6 mm, including a dedicated optical coating optimized for the OCT operating wavelength range. The optical elements were supplied together with a complete inspection and metrology package in order to verify their suitability for integration into the laser scanner optical path. The inspection included dimensional verification, surface flatness measurements, surface quality evaluation, parallelism measurements, and coating transmission characterization.

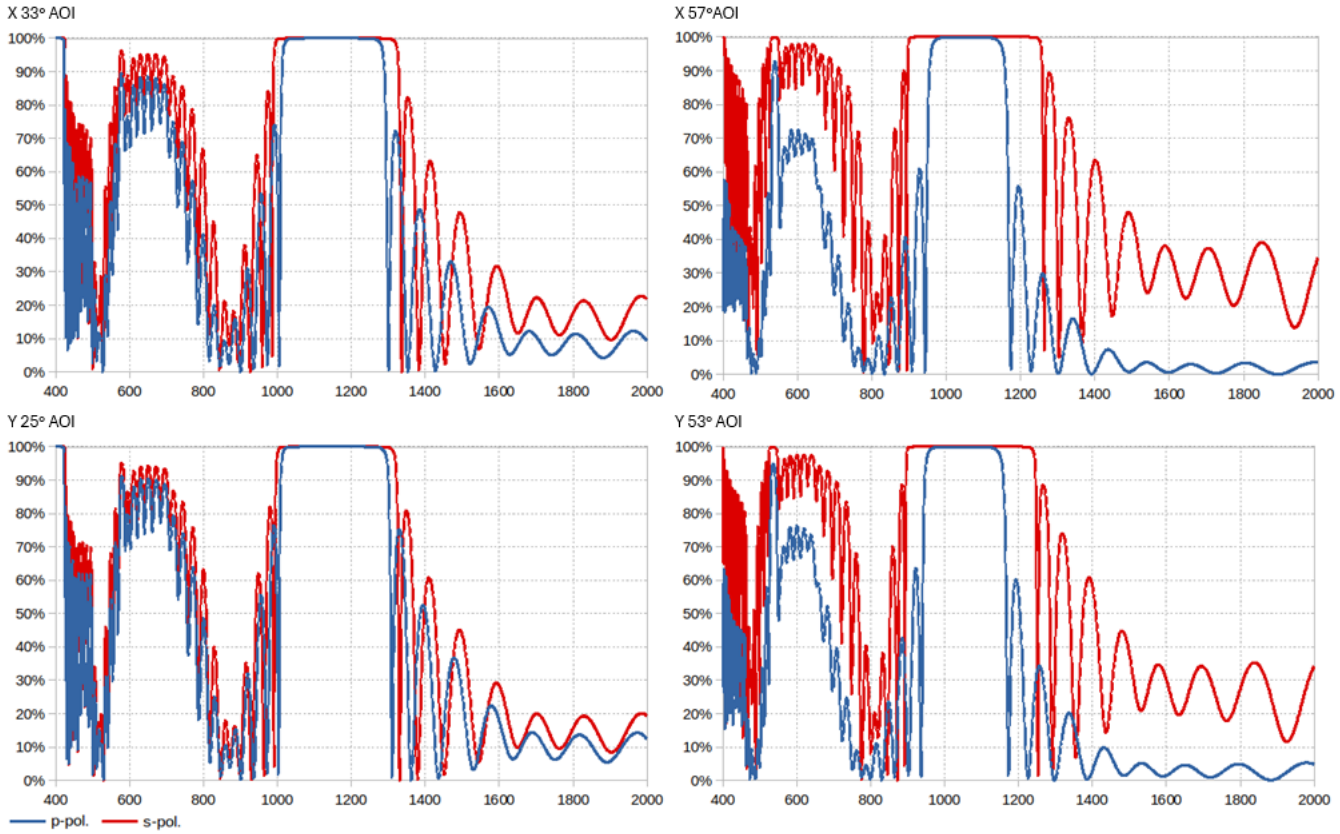

Figure 8: OCT source wavelength

Several interferometric surface maps and wavefront measurements were performed for each optic using Zygo interferometry. The obtained results demonstrated surface flatness values in the range of approximately λ/5 to λ/8 PV, with low RMS wavefront error, indicating good optical quality and acceptable surface uniformity for beam transmission applications. The measurements also confirmed that the optics maintained high parallelism (below 3 arcmin specification), which is important in order to minimize beam deviation and distortion when inserted into the optical path. In addition, transmission measurements of the optical coating were carried out in order to evaluate compatibility with the OCT source wavelength. The transmission curves showed high transmission in the 820–860 nm region, reaching approximately 89–91% transmission around the OCT operating wavelengths.

During the integration and evaluation phase, the team investigated the possibility of implementing an OCT-based monitoring solution through the scanner optical path for real-time keyhole depth measurements during laser processing. However, experimental evaluation and transmission analysis demonstrated that the scanner optical path introduced significant attenuation of the OCT signal. In particular, the operating wavelength of the OCT source (~850 nm) coincided with a low-transmission region of the scanner mirror coating characteristics.

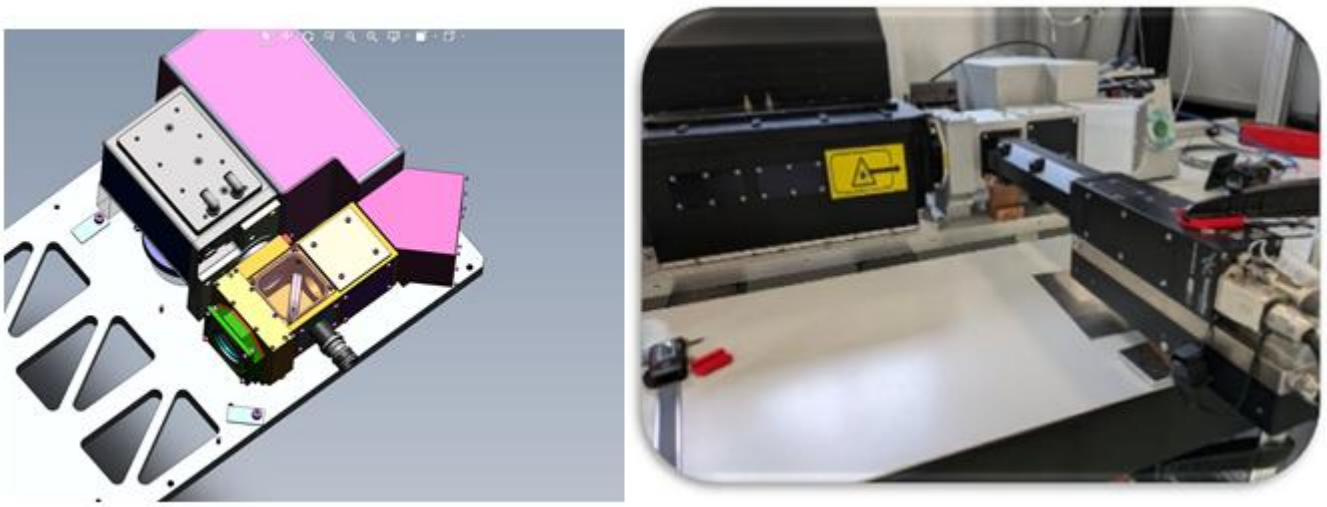

Figure 9: Mechanical design (left) and physical integration (right) of the OCT system

As a result, the OCT beam intensity after passing through the scanner became insufficient for stable and reliable acquisition of keyhole depth measurements. Therefore, although the optical components themselves met the required manufacturing and geometrical specifications, the overall OCT implementation through the current scanner configuration was found to be unsuitable due to optical transmission limitations of the scanner mirrors at the OCT wavelength range.

This work nevertheless provided important experimental validation and helped identify the key optical limitation in the system architecture. The activity also established a verified optical characterization methodology and generated practical knowledge for future integration of in-process monitoring solutions using alternative wavelength ranges or modified scanner coatings.

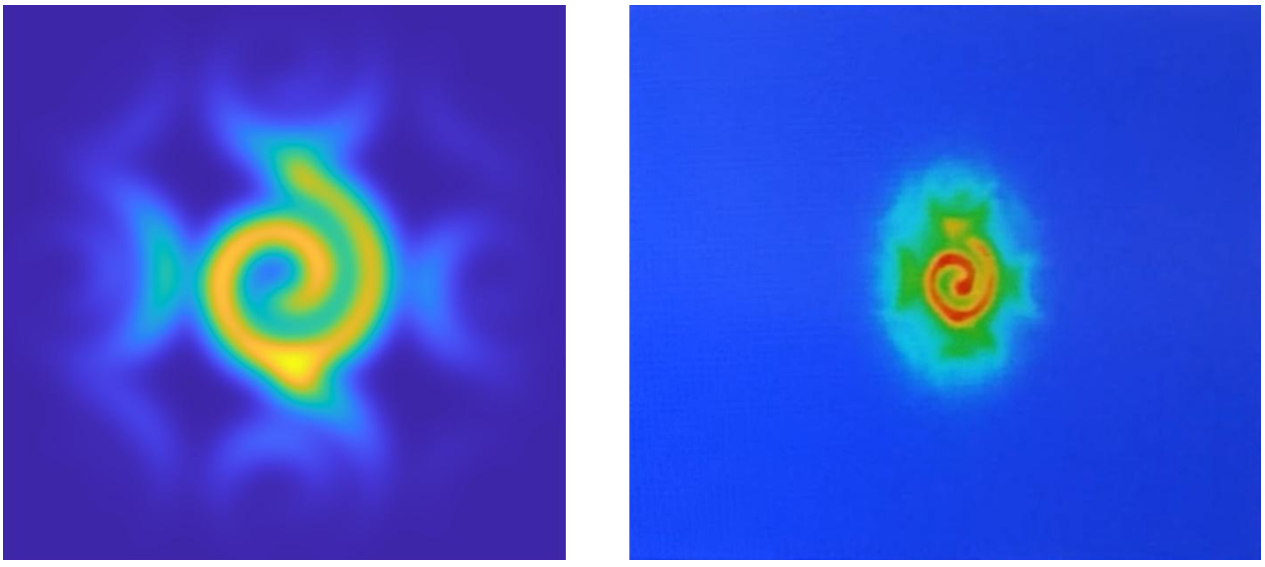

Figure 10: Left - nominal shape. Right - beam shape collected by the beam shape camera

4.2. Machine-related sensors

4.2.1. Machine monitoring sensors: beam shape camera

A beam shape camera is used to monitor the spatial intensity distribution and quality of the laser beam in real time. The selected camera is the IDS GV-5880CP-M-GL, which incorporates a Sony IMX178 monochrome CMOS sensor based on STARVIS back-side illuminated (BSI) technology, enabling enhanced light sensitivity and reduced read noise during low-light image acquisition. The sensor provides

a spatial resolution of 3088 × 2076 pixels with a pixel size of 2.4 µm × 2.4 µm and an optical format of 1/1.8". The imaging architecture operates using a rolling shutter with global-start functionality and progressive scan readout. The camera supports 12-bit monochrome image acquisition and achieves frame rates of up to 18 fps at full resolution through a GigE Vision compliant 1 Gbps Ethernet interface. The data is processed and made available to the Lasers4MaaS platform to monitor: (1) beam profile image; (2) trend graph of beam diameter or centroid drift over time. This will be demonstrated in WP15 and WP16.

4.2.2. Machine monitoring sensors: laser analogue power

The laser analogue power monitoring system measures the real-time output power of the laser using analogue sensor signals integrated into the machine control system. The PD300R photodiode sensor data is streamed to the Ophir EA-1 card which is then transferred to the local PC (data formats are described in the next chapter of the deliverable). The sampling rate is 10-15 data points/s with an analogue voltage [0, 10]V at full scale. The PD300 is assembled after the low power bender (in the closed-loop) in the same housing of the beam shape camera.

At the same time the SmartMOVE scanner laser output (input to the laser) is recorded and sent to the DAQ for processing.

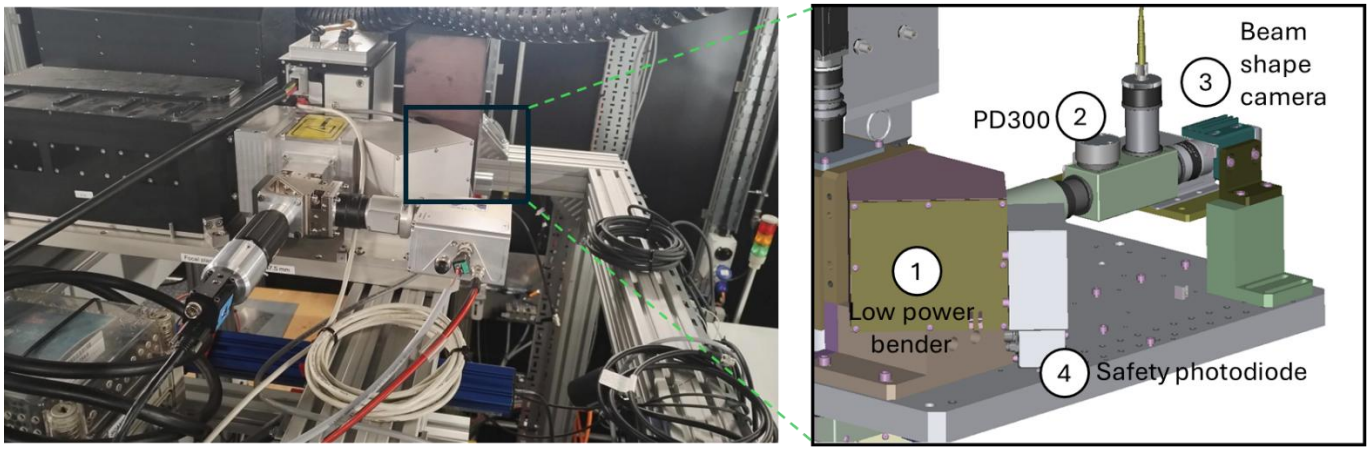

Figure 11: The laser analogue power monitoring system

The data is processed and made available to the Lasers4MaaS platform to monitor to monitor power trend graph over time. This will be demonstrated in WP15 and WP16 to verify that the laser operates within specification, detect degradation or abnormal laser behavior, improve process repeatability and product quality, support machine diagnostics and preventive maintenance.

4.2.3. Machine monitoring sensors: flow meters

To analyse overall pneumatical energy consumption, appropriate sensors were installed on the HIP (Hall Installation Plate), which ensures the general air supply to the plant. The sensors are divided between the compressed air supply for the laser technology equipment and the fixture technology. The sensors are connected to the plant control system using an IO-Link module, enabling data to be recorded via the PLC ProfiNET network. Data can be stored by time interval, process or component. The following sensors are used:

- Pressure meter: SPAU-P10R-W-G18FD-L-PNLK-PNVBA-M12U
- Flow meter: SD9500 SDR32DGXFRKG/US-100
- IO-Link module: BNI PNT-508-105-Z031

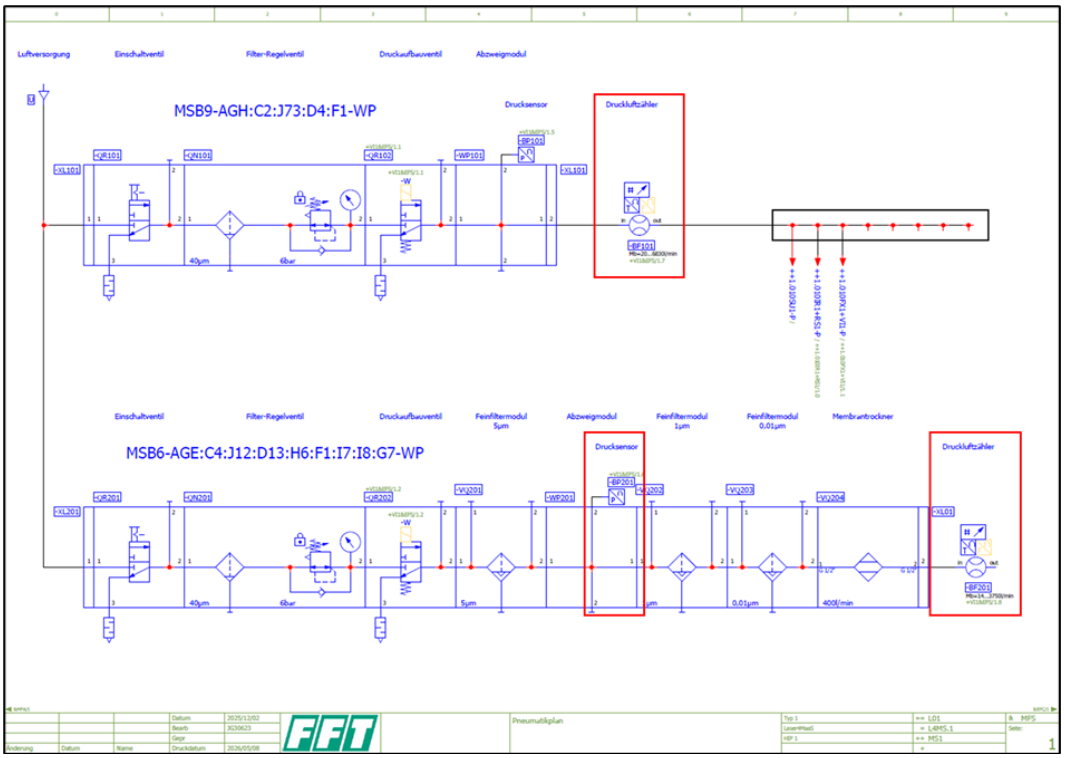

Figure 12: Pneumatical energy consumption system

4.2.4. Machine monitoring sensors: energy meters

The equipment in the main power cabinet was designed to monitor energy consumption, which is also used for the LCA. The components are divided into main switch and data acquisition equipment as follows. Data can be stored by time interval, process or component via ProfiNET communication.

- Main switch: Siemens 3VA2216-7KP32-0AA0
- Communication module: Siemens 3VA9187-0TB10
- Data concentrator: Siemens 3VA9987-0TA20
- Switched Ethernet Profinet Module: Siemens 7KM9300-0AE02-0AA0

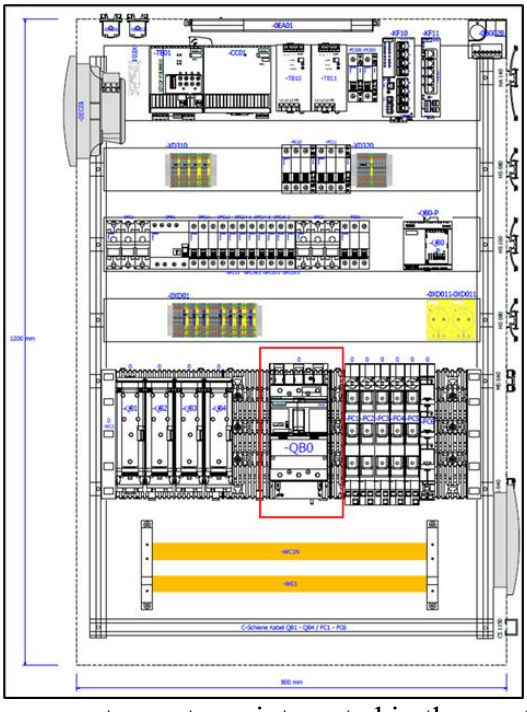

Figure 13: Energy meter systems integrated in the master PLC board

5. T11.2 Testing of sensors and characterisation of KPIs, integration and data acquisition system

5.1. Data policy and data synchronisation

To support the Lasers4MaaS digital manufacturing environment, a dedicated data acquisition and synchronization architecture was defined for collecting, buffering, transferring, and storing process data generated during laser operation. The objective of the implemented framework is to enable reliable traceability of manufacturing sessions while allowing future integration of advanced monitoring, analytics, and AI-based optimization tools, including remote monitoring and predictive maintenance.

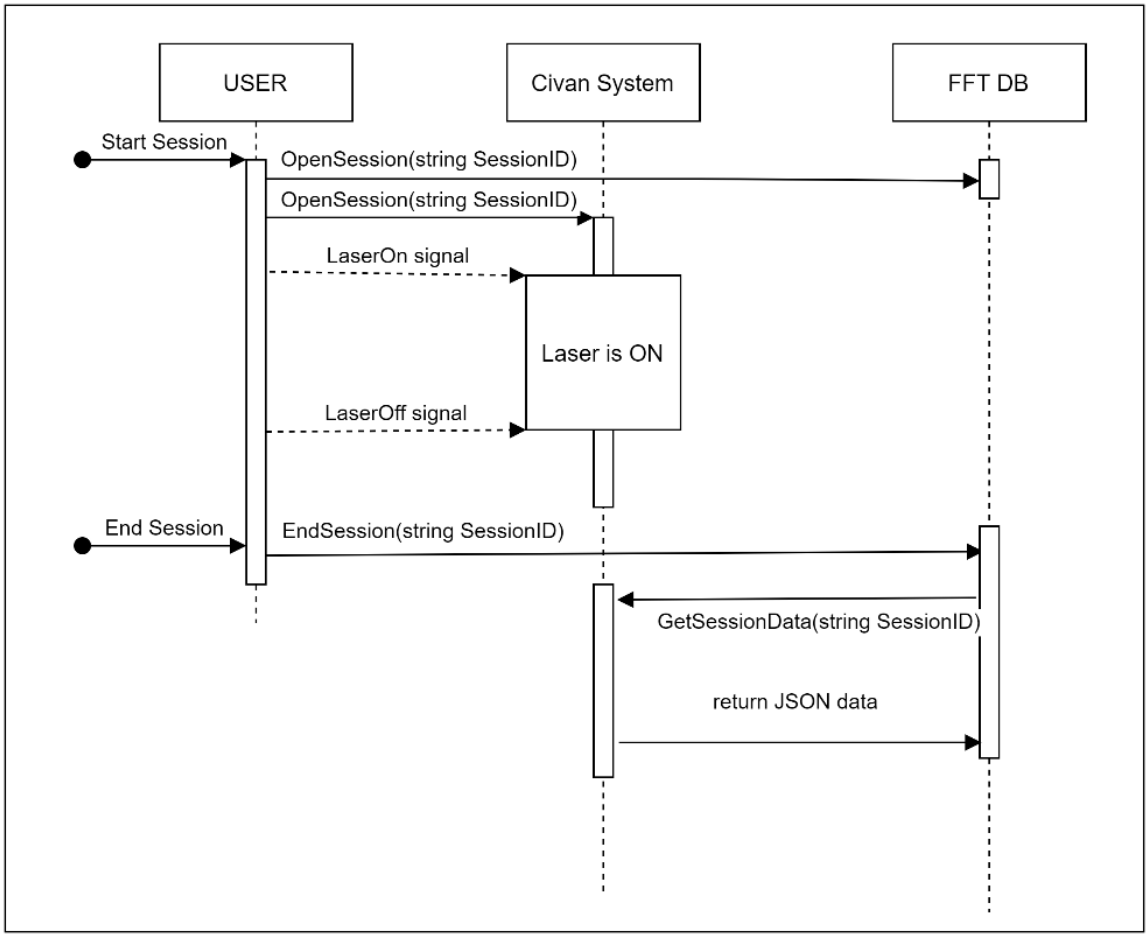

Figure 14: Data policy and data synchronization overview

The developed architecture establishes communication between three primary system entities: (1) User / operator interface; (2) laser control system; (3) production plant database platform.

The overall concept is based on a session-oriented workflow in which each manufacturing process is associated with a unique SessionID. This identifier allows synchronization between the laser controller, scanner system, monitoring devices, and the external database infrastructure. At the beginning of each process, the operator initiates a new manufacturing session by sending an OpenSession command simultaneously to both the Civan laser system and the FFT database. Once activated, the laser controller initializes internal memory buffers and prepares all relevant acquisition channels for real-time data collection. During active laser operation, the system continuously gathers and buffers multiple process-related data streams, including internal camera images, coaxial camera images, laser monitored power levels, scanner operational data, process timestamps and session metadata.

The collected information is temporarily stored locally during the manufacturing process in order to avoid unnecessary network traffic and to ensure stable acquisition rates during operation. Once the manufacturing

session is completed, an EndSession command is issued. At this stage, the local FFT/WMG database requests the complete session dataset from the DBS system. The laser controller compiles the buffered process information into a structured JSON payload and transfers it to the database for permanent storage and future analysis. The synchronization mechanism was designed to support different sensor modalities and heterogeneous data types. The current implementation already supports: (1) numerical sensor data; (2) scanner telemetry; (3) power monitoring logs; (4) image-based monitoring channels. Camera images are transferred in PNG format using Base64 encoding to ensure compatibility with the platform infrastructure and future cloud-based analytics environments.

The data policy is separated in time-series and event-based data, ensuring consistent traceability and efficient storage. Sensor signals from production are captured either with a defined sampling rate and a single start timestamp or with individual timestamps per data point. This enables flexible synchronization across systems. All data will be linked to a unique PartID to guarantee traceability throughout the production process. System-wide consistency between PLC, sensors, and external subsystems will be ensured by a time synchronization. To control storage requirements, image data is not included in the main payload but referenced externally, with dedicated APIs enabling on-demand retrieval. Furthermore, the data structure is designed in a modular and extensible way, allowing future extensions (e.g., new parameters or varying sampling rates) without breaking compatibility.

In addition, a configurable FIFO (First-In, First-Out) retention strategy was implemented in the local laser controller to manage temporary storage efficiently. The system currently maintains a configurable number of recent sessions locally until successful synchronization with the FFT database is completed.

The implemented framework creates the basis for future integration of additional sensing technologies and advanced monitoring solutions within the Lasers4MaaS platform. The modular architecture enables future expansion towards: melt pool monitoring, thermal imaging systems, beam diagnostics, process quality monitoring, AI-driven process optimization, predictive maintenance analytics, cross-platform manufacturing traceability.

5.2. Data acquisition systems

The WMG setup uses a National Instruments (NI) DAQ device, specifically the NI USB-6363. This multifunction DAQ device provides up to 32 analogue input channels (16 channels differential) with 16-bit resolution and a maximum aggregate sampling rate of 2 MS/s, enabling simultaneous high-speed multi-channel acquisition. The device also includes 4 analogue output channels (up to 2.86 MS/s aggregate), 48 digital I/O lines, and four 32-bit counter/timers for timing, triggering, and event counting. For the present configuration, we have assumed up to 8 analogue input channels (5 in use for each identified sensor – see Table 1; and 3 spare) are sampled at 50 kHz per channel with 16-bit resolution, resulting in an aggregate data throughput of approximately 0.8 MB/s (8 × 50k samples/s × 2 bytes/sample). This data rate is within the capabilities of the USB 2.0 interface (with a nominal maximum of 60 MB/s). Acquired data is streamed in buffered blocks to a local DAQ-PC, where it is processed in real time using a MATLAB-based application environment. The selected DAQ-PC is the ONLOGIC Helix 52.

At FFT/ECOR, the data acquisition architecture is based on a distributed approach combining PLC, industrial edge devices, and dedicated subsystems such as the Civan laser system, with FFTrace acting as the central traceability layer. Sensor and process data are collected from multiple sources, including cameras, laser source, scanner, and robot, and aggregated on an industrial PC, where they are synchronized and linked to the corresponding PartID. The aggregated data will be transmitted in a defined JSON structure via MQTT or OPC UA interfaces to FFTrace to capture production events. Scanner and laser-related data are preferably collected and integrated into the same dataset to ensure consistency. The architecture supports both time-based and event-based acquisition and is explicitly designed for scalability and extensibility, e.g., by supporting different sampling rates and future system enhancements.

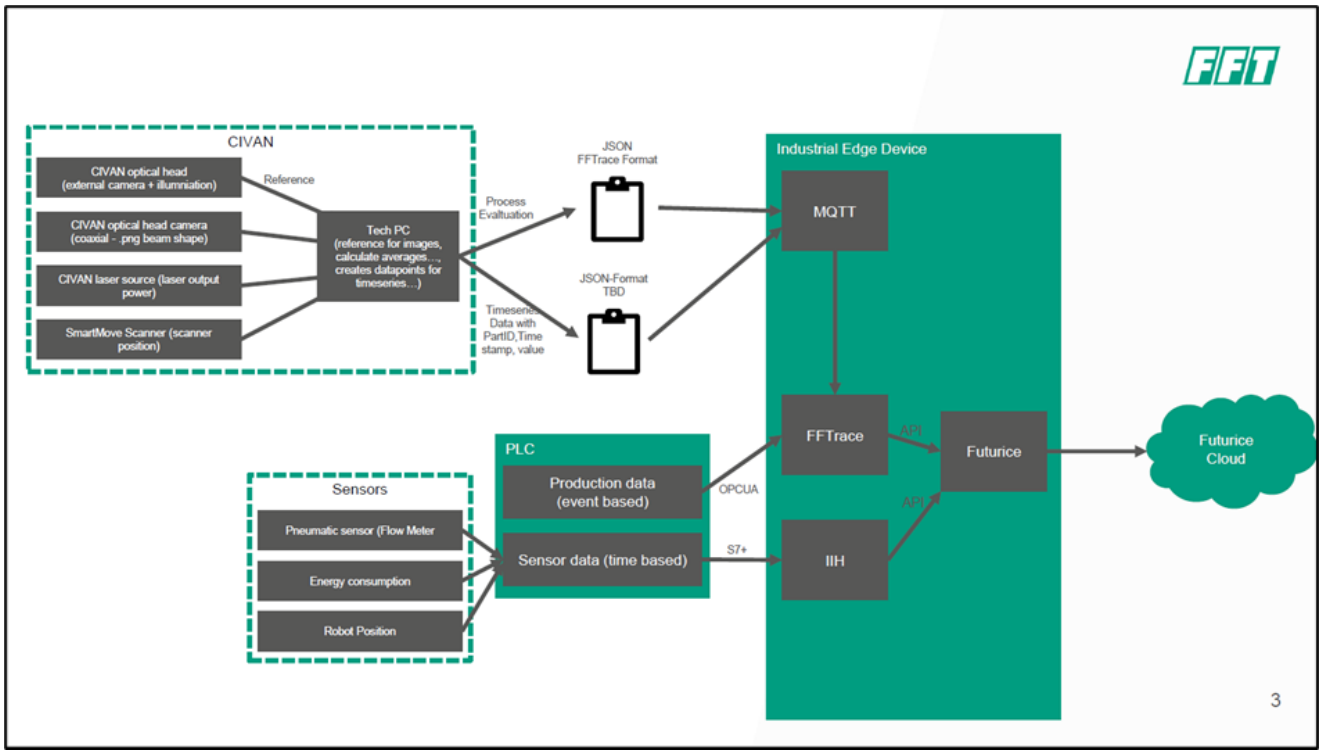

Figure 15: Data acquisition system - production intent

5.3. Characterization of sensors

The following section provides example of data processing and relationship to weld features.

Off-axis optical microphone

Tests were conducted to characterize the background noise and the process emissions registered by the microphone when varying the airblade position. The noise sources included shielding gas, cross jet mounted on the laser welding head, fume extractor and the airblade itself. The signals were characterized both in time domain and in frequency domain. The investigation of the frequency properties of the acoustic signal was helpful in finding out the frequency distributions of the signal emitted by the process with and without the background noise.

Power Spectral Density (PSD) analysis was performed on the full acoustic signal to determine the frequencies at which the dominant disturbances acted and their corresponding intensities, thereby enabling assessment of the influence on background noise. In parallel, the noise-filtered acoustic emission was analyzed to identify the characteristic frequencies associated with the laser-induced process emissions. The PSD analysis was conducted with Welch-Barlett method to denote the power of the signal versus its frequency. This approach is based on the periodogram method, which transforms the signal from the time domain to the frequency domain, but improves it by averaging multiple periodograms over time, thus reducing the variance of individual power estimates. In this study, a rectangular window of 1000 sampling points with 50% overlap was used, and the discrete Fourier transform was computed over 4096 points. The rectangular window allowed for both high frequency and magnitude resolution.

After isolating in the time domain, a region of interest, ROI_p, and a region containing only background noise, ROI_{bg}, (blue and red area, respectively, in the figure below), the signal-to-noise ratio (SNR) was calculated to assess the influence of background noise on the acoustic signal as the airblade position varied. The ROI was defined between 20% and 80% of the time window in which the laser was active. The resulting values of SNR were close to zero, meaning the noise was almost overlapping the signal during the process. In this respect, three denoising techniques were selected on ROI_p for their proven effectiveness on non-stationary acoustic emission signals: wavelet denoising, spectral subtraction, spectral gating and wiener

filtering. The resulting SNRs were compared. By a closer analysis of the PSD for all signals, it was evident that the only frequency window where the signals of the background noise and the process were not overlapping was 2-25 kHz. Hence, in order to link the process emissions with the signal acquired, a bandpass filter was applied on those frequencies to calculate $RMS_{p,mic}$. To quantify the acoustic energy associated with the welding process independently of the absolute noise level, a Process Power Index (PPI) was introduced. The PPI was defined as the ratio between the signal energy measured in the ROI_p and the energy of the background noise measured in the ROI_{bg}. A value of PPI > 1 indicates that the acoustic energy during the process exceeds the background, whereas PPI ≤ 1 suggests that the process contribution is weak or masked by background noise.

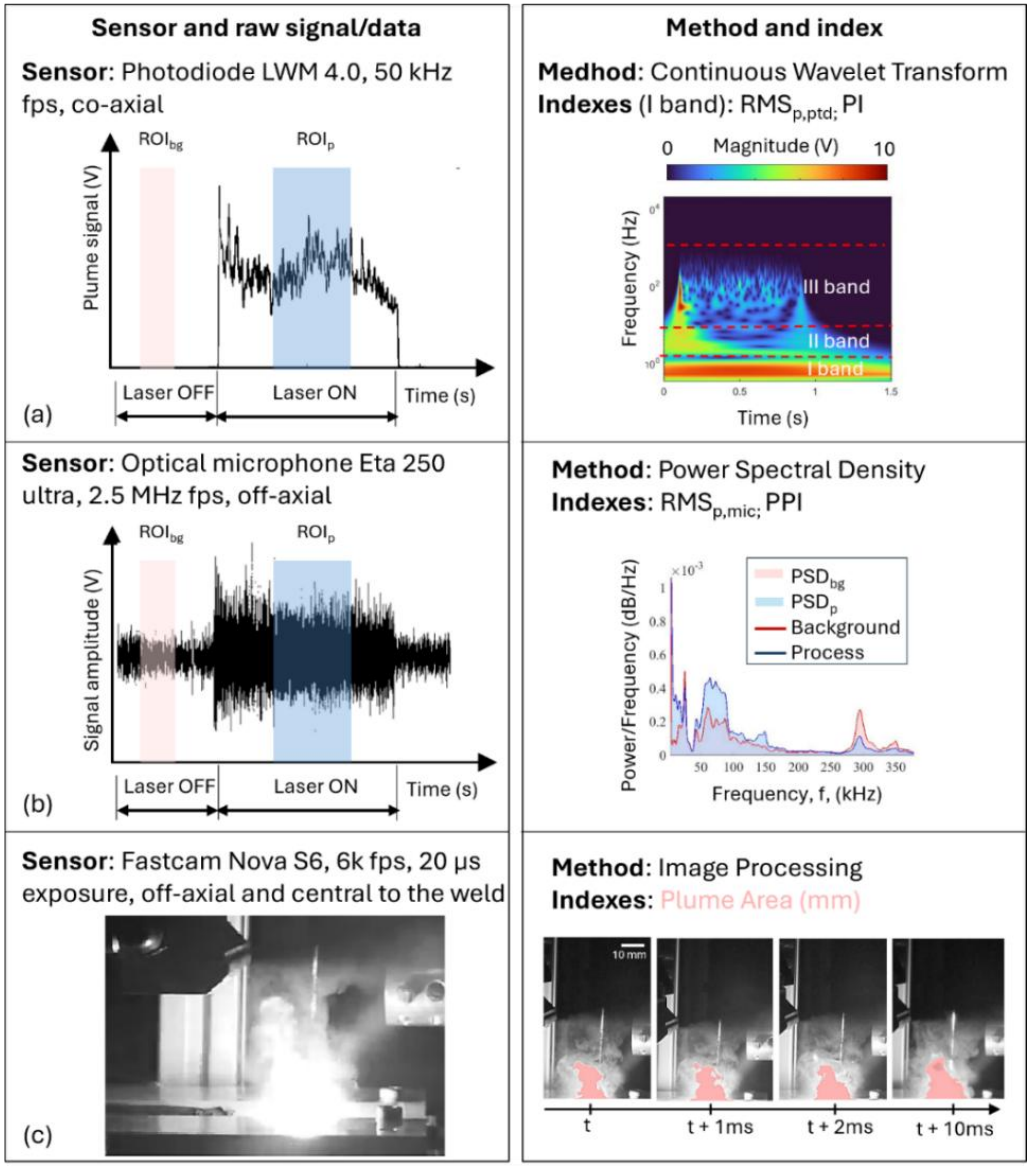

Figure 16: Data processing pipeline of the selected sensors.

Photodiodes

Among the three signals collected by the LWM sensor, only the one associated with the UV and visible radiation (~350-700 nm) bandwidth was analyzed since it directly correlates to the plume intensity. Both temporal and spectral analysis were performed using continuous wavelet transform (CWT) using the built-in signal processing tools available in MATLAB. The morse function was implemented for the wavelet transform, with parameters $\gamma = 3$ and $\beta = 30$. These specific parameters were selected to prioritize frequency resolution over temporal resolution. This balance was determined and validated through a preliminary sensitivity analysis. For all the tests performed, the CWT revealed three characteristic frequency bands. Similarly, for microphone data processing, the region of interest ROI_p was extracted to isolate the signal

content within the selected frequency bands during the steady-state phase of the process. In order to quantify the average signal energy within the selected time-frequency region, the $RMS_{p,ptd}$ index was calculated for each band across all frequencies of the signal. The influence of the airblade position and process parameters were assessed using the Plume Index, PI.

High-speed camera

The high-speed recordings of the welding process were analyzed through a MATLAB script to quantify the temporal evolution of the plume above the weld pool. The analysis was restricted to the central portion of the recorded process, corresponding to 20–80% of the total recorded frames, to exclude the transient start and end phases of the welding task. Each video consisted of a sequence of TIFF images acquired at 6000 fps, with an exposure time of 20 µs and a spatial resolution of 1024 × 640 pixels. For each video frame, the plume region was identified through a thresholding process that selected only the brightest pixels, specifically those exceeding 95% of the maximum intensity value. The resulting binary mask represented the detected plume for each analyzed frame, and its area was quantified by counting the number of pixels, which was then calibrated using a spatial scale of 4 pixels/mm. The 95% threshold value was empirically determined by iteratively adjusting the threshold and visually inspecting the resulting segmentation overlaid on the original video frames. This value was selected as it provided the most accurate delineation of the brightest plume region (*vapor zone*) when compared to the experimental videos. It was assumed that measuring the hot metal vapor zone could provide an indication of the extent to which subsequent condensation would develop into the more absorptive dense cloud of particle zones. The Coefficient of Variation (CoV) was used to quantify plume stability. Since the CoV represents the ratio between the standard deviation and the mean value of the plume area, higher values indicate stronger temporal fluctuations and therefore a less stable plume.

5.4. Testing of sensors

High-speed imaging and weld depth analysis

The influence of airblade position on plume emission and resultant weld geometry (weld depth and width, and weld area) was investigated through a combined qualitative and quantitative analysis. The qualitative assessment compared weld cross-sections with corresponding high-speed video frames. Each frame shows three distinct emission regions: (1) a broader, elongated bright region following the laser itself; (2) a diffuse, lower-intensity halo extending outward, associated with fume generation and plume expansion; (3) a highly shining area just above the interaction point, where the laser is focused on the material. When a laser power of 2 kW is applied, the airblade position shows neglectable influence on weld penetration or weld area, except at the lowest height z_b = 10 mm. At higher energy inputs, reducing the airblade height z_b visibly flatten the plume and enhances weld penetration, suggesting that effective plume control is critical at higher energy inputs.

To quantify these effects, the mean plume area and its coefficient of variation (CoV) were derived from high-speed video data. The mean plume area of all experiments shows that when the airblade is turned off (gray dotted line) the increase in laser power from 2 to 5 kW leads to a significant enlargement of the plume area, indicating a higher amount of vaporized material and ejected particles. Activating the airblade in close proximity to the interaction zone (z_b = 10 mm) suppresses the plume across all power levels, suggesting the airflow capacity to confine and deflects the vapor plume. Conversely, the largest plumes were observed at high laser power with the airblade positioned further away (z_b = 60 mm), where its confining influence is minimized. To quantify the influence of each parameter on plume fluctuations, CoV values were reported. The analysis revealed that plume stability is governed by an interaction between laser power and airblade position. At low power (2 kW), the plume is highly unstable, with CoV values peaking at 0.59 and 0.88 for x_b = 80 mm and 160 mm, respectively. Increasing the laser power to 4-5 kW significantly reduces the CoV to approximately 0.27–0.29, suggesting a more stable and continuous vapor generation. Moreover, when the airblade is positioned very close to the interaction zone (z_b = 10 mm), the plume area becomes extremely

small due to the strong confinement imposed by the airflow. Under these conditions, even small temporal variations produce relatively high CoV values, indicating a thin but highly fluctuating plume structure.

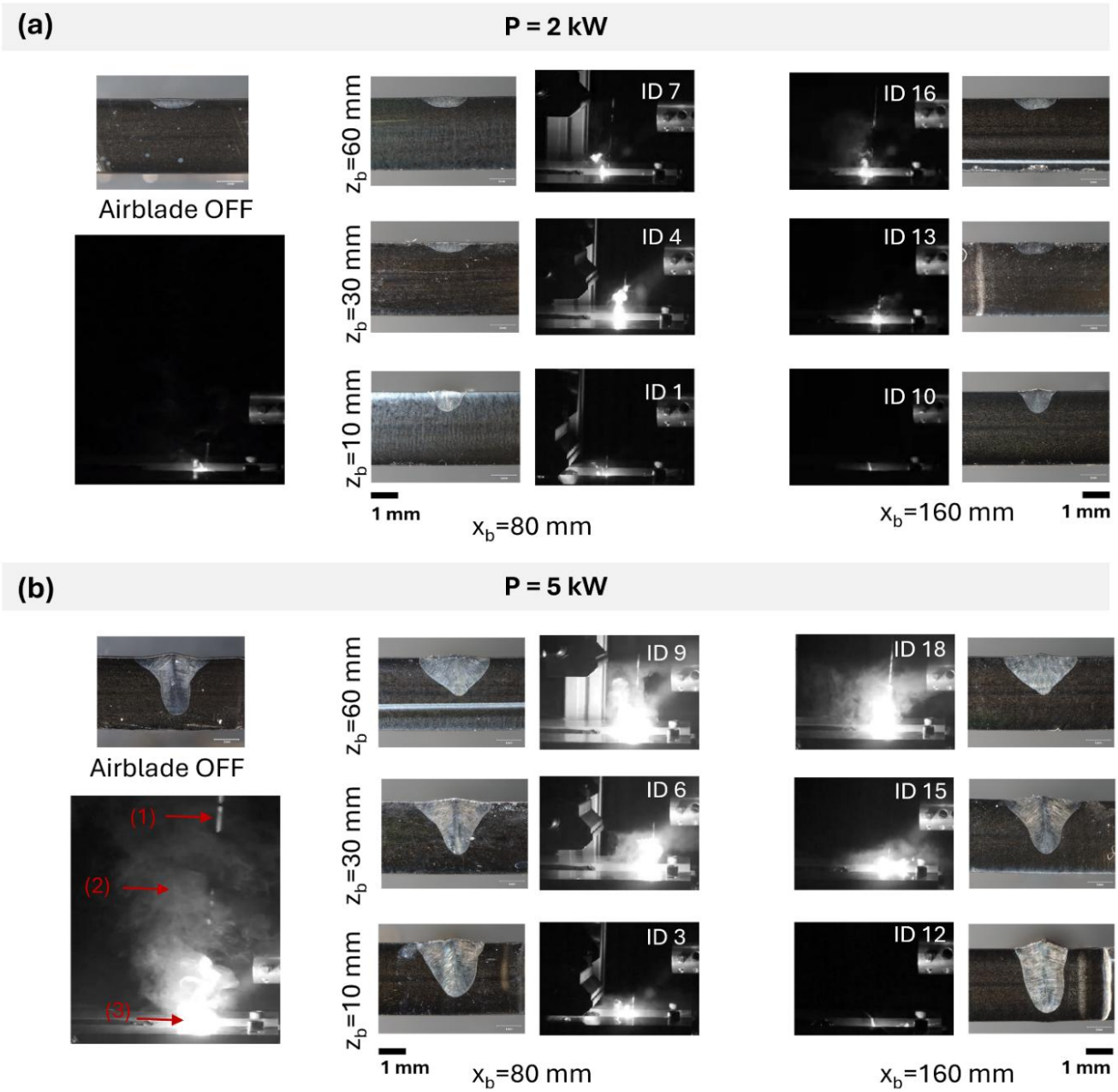

Figure 17: Influence of airblade position on plume formation and resulting weld depth.

Conversely, larger plume areas are generally associated with lower CoV values, reflecting a more continuous vapor emission regime. Longitudinally (x_b-direction), moving the airblade from 80 mm to 160 mm reduced the mean plume area of about 21%. The vertical position (z_b-direction) had a far stronger effect: lowering the airblade closer to the workpiece (from z_b = 60 mm to 10 mm) resulted in a 91% reduction in plume area, confirming that a close proximity to the workpiece (z_b = 10 mm) provides the most effective suppression. This trend is directly mirrored in weld depth measurements. Longitudinal position had a minor effect, with mean weld depth increasing of only 15% over the same range. In contrast, lowering z_b from 60 mm to 10 mm increases mean weld depth by approximately 57% (from 1.16 mm to 1.82 mm), while the standard deviation drops to about 28% (from 0.1 mm to 0.07 mm). This optimal configuration for both plume suppression and weld depth (x_b = 160 mm, z_b = 10 mm) also significantly outperforms the airblade off condition, increasing weld depth by 125% at 2 kW (from 0.4 to 0.9 mm) and 12% at 5 kW (from 2.6 to 2.9 mm). In conclusion, the combined data acquired from high-speed camera and the measured weld depth provides direct evidence that the airblade' s efficacy is highly dependent on its spatial

configuration. An optimal configuration was identified (x_b = 160 mm, z_b = 10 mm), as it concurrently enabled maximum plume suppression and the greatest weld depth. The vertical positioning z_b was found to be the dominant factor governing plume suppression, albeit when setting high energy input, longitudinal position optimization becomes also essential to maintain process stability. The significance of these specific spatial configurations is further corroborated in the subsequent sections through dedicated signal processing.

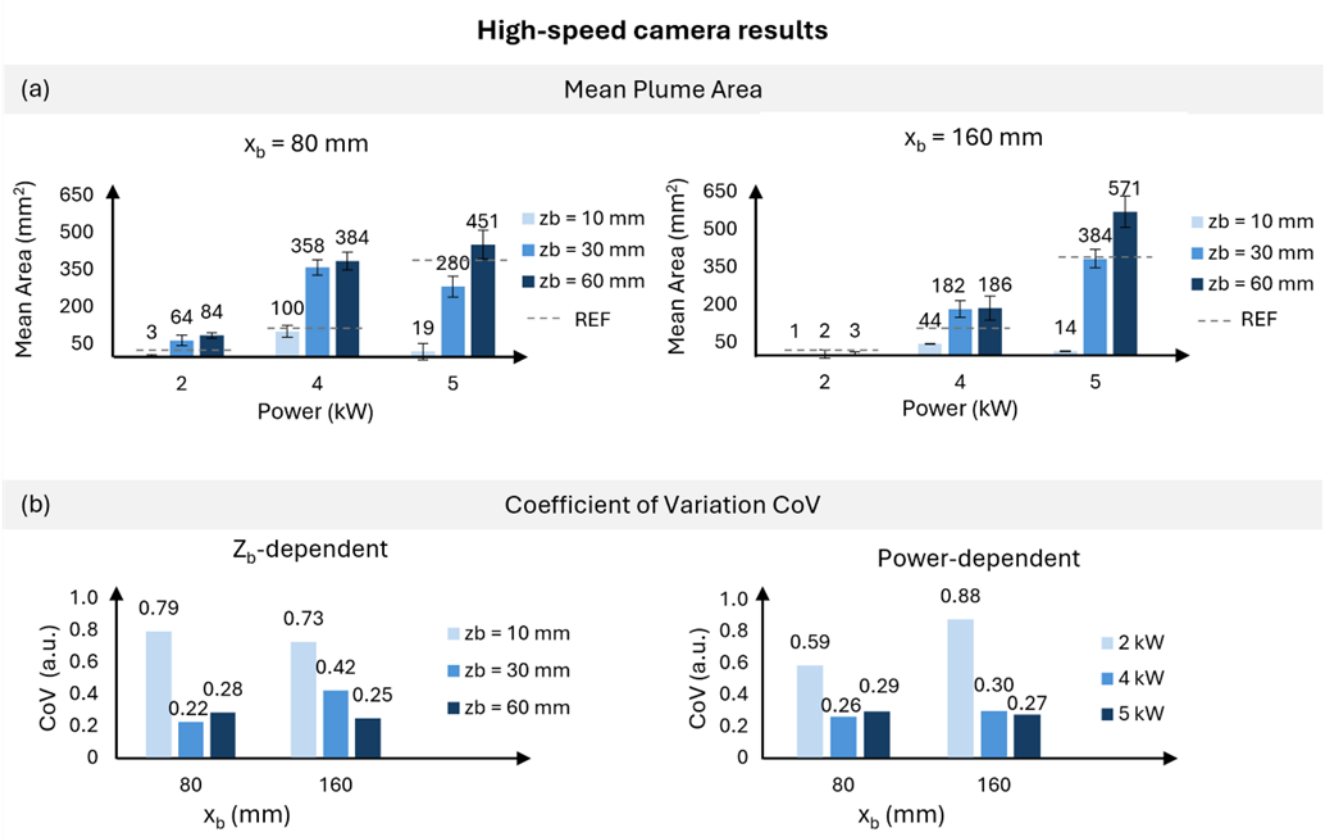

Figure 18: Plume intensity analysis.

Photodiode analysis and results

The plume signal acquired by the photodiode sensor was analyzed. First, a wavelet analysis was performed on all data streams to reveal distinct spectral signatures correlating with both plume intensity and its dynamic fluctuations. All recorded signals exhibit an initial phase of high-energy activity, corresponding to keyhole formation. Its intensity and spectral extension vary significantly depending on the power applied and airblade position, a dependency consistent with established literature.

To quantitively evaluate these spectral features, three characteristic frequency bands were defined: Band I (0–1 Hz): this lower frequency range captures the quasi-stationary component of the photodiode signal, representing the average intensity level or slow variations of the emitted or reflected light during the welding process. Band II (1-10 Hz): this band reflects slower process fluctuations. Band III (10-14000 Hz): this band encompasses the fast, dynamic components directly associated with plume formation and vaporization instabilities.

The $RMS_{p,ptd}$ value of the wavelet coefficients was calculated to quantify the average signal energy, or mean power, within each specific time-frequency region. Analysis of the baseline trials, conducted without the airblade, reveals a clear trend: across all three frequency bands, the $RMS_{p,ptd}$ values increase with laser power (represented by the REF dotted lines in Figure 19*)*. This indicates the development of a more intense and unstable plume, consistent with the expectation that higher power input leads to greater material

vaporization, resulting in a denser plume and stronger oscillations. This power-dependence rise is particularly pronounced in Bands I and II. As previously observed in the high-speed camera data, the effect of power on plume luminosity becomes less significant above 4 kW, except for the z_b = 60 mm configuration where the airblade is ineffective.

In contrast, the high-frequency components in Band III exhibit markedly different behavior. Here, the $RMS_{p,ptd}$ values remain comparatively low and show little dependence on laser power. This suggests that the high-frequency fluctuations are intrinsic to the plasma/scattering phenomena and do not scale proportionally with the energy input. The efficacy of the airblade was evaluated using the $RMS_{p,ptd}$ values, with the results for the I band presented in Figure 19*a*.

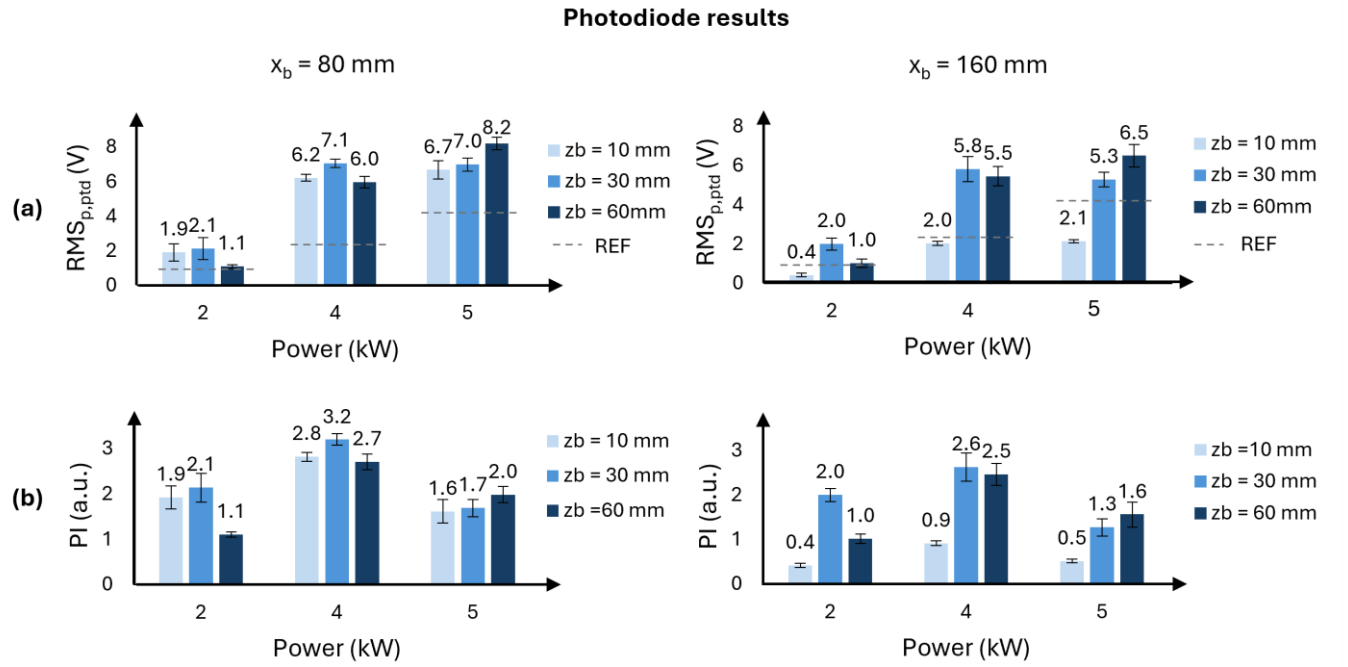

Figure 19: Results of photodiode sensing.

The reference condition (REF) is the one with the airblade OFF. Another way to visualize the impact of airblade position and laser power across all tests is through the Plume Index (PI), calculated as the ratio between the heigh of each bar in Figure 19*a* ($RMS_{p,ptd}$) and the heigh of the corresponding baseline condition outlined by the REF dotted line ($RMS_{noblade}$). As outlined in Figure 19*b,* when the airflow is emitted close to the welding zone at x_b = 80 mm, PI exceeds a value of 1 across all three bands at every laser power level. This suggests that, at this specific configuration, the airblade not only fails to deflect the plume, but actively amplifies its fluctuations, resulting in greater temporal variability than the baseline condition. This counterproductive result is likely due to the interaction between the airblade and the shielding gas covering the weld. The externally applied airflow is postulated to disrupt the laminar flow of the shielding gas, compromising its coverage and leading to increased atmospheric contamination and process instability, which is then captured by the photodiode as a more intense and fluctuating signal.

In contrast, the most effective plume suppression, as confirmed also by high-speed camera data, is achieved with the airblade positioned downstream and closest to the workpiece (x_b = 160 mm, z_b = 10 mm). Here, the $RMS_{p,ptd}$ bars in Figure 19 remains consistently below the reference line (PI < 1), confirming superior stability. The performance of this optimal configuration stands in stark contrast to ineffective ones, such as x_b = 80 mm z_b = 30 mm at 4 kW, where a PI of 3.2 signifies a 220% increase in signal intensity. Collectively, the results from the high-speed imaging, weld depth analysis, and photodiode signals demonstrated a clear correlation between plasma plume emission and weld depth penetration.

Optical microphone and results

Initial analysis confirmed a high level of noise interference. The original data showed a SNR as low as -0.76 dB, with the RMS amplitude in the process region ($RMS_{p,mic}$) being 17% lower than in the background noise in RMS_{bg}. Among tested denoising techniques, spectral subtraction and wavelet filtering did not significantly improve the SNR, while Wiener filtering increased it up to 9.8 dB. However, this improvement was not consistent across all samples, suggesting that noise and signal components overlap in frequency, making filtering strategies risky as they can distort the useful signal.

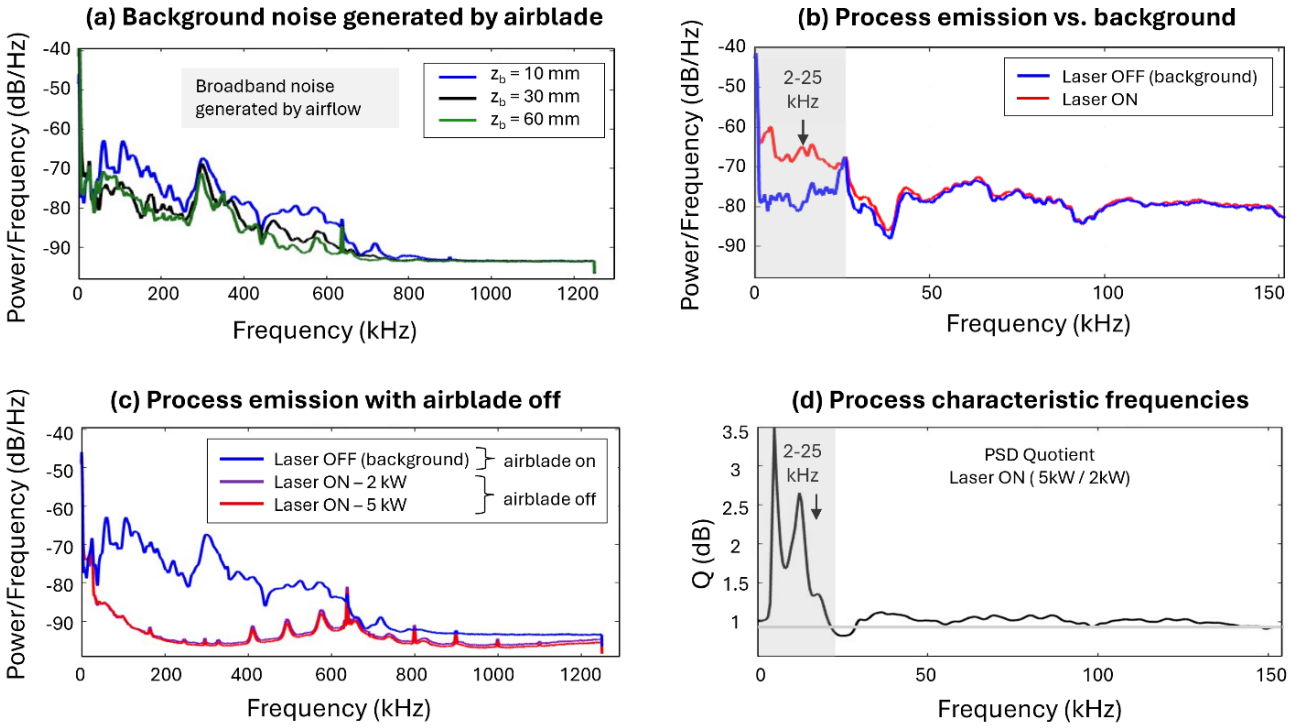

Figure 20: Acoustic emission spectra measured with the optical microphone.

Power spectral analysis was used to evaluate the effect of airblade activation on the acoustic response. Results showed that airblade's airflow introduces broadband noise extending across the entire frequency range, which becomes negligible above approximately 800 kHz for all configurations. Consistent with the findings reported in the literature, the signal intensity was found to be strongly dependent on the sensor positioning. Specifically, as illustrated in Figure 9a, when the airblade was positioned at x_b = 80 mm, the z_b = 10 mm configuration (blue line) exhibited a higher spectral intensity across most of the spectrum.

To quantify spectral differences between two signals, the PSD quotient Q [dB] was calculated as $Q = 10\log_{10}(PSD_1/PSD_2)$, where PSD_1 and PSD_2 are the two spectra under comparison. This metric highlights frequency bands where acoustic emissions differ most, identifying the characteristic frequencies at which the process emits acoustic energy. To isolate process-related frequencies, Q was computed as the ratio between the process PSD and the background noise PSD (Figure 9b). The analysis consistently identified the 2-25 kHz range as the primary region where process emissions dominate over the background. The selection of this specific band was directly derived from the quotient analysis, as it represents the frequency interval where Q > 0 dB across all tested configurations. As illustrated in Figure 21c, within this band, distinct peaks at 4 kHz and 12 kHz were found to intensify with rising laser power, further confirming their direct correlation with process energy. These findings aligns with prior studies by Farson et al., who observed consistent energy differences in the 1-2 kHz bands when comparing spectrograms for full and partial penetration welds [40].

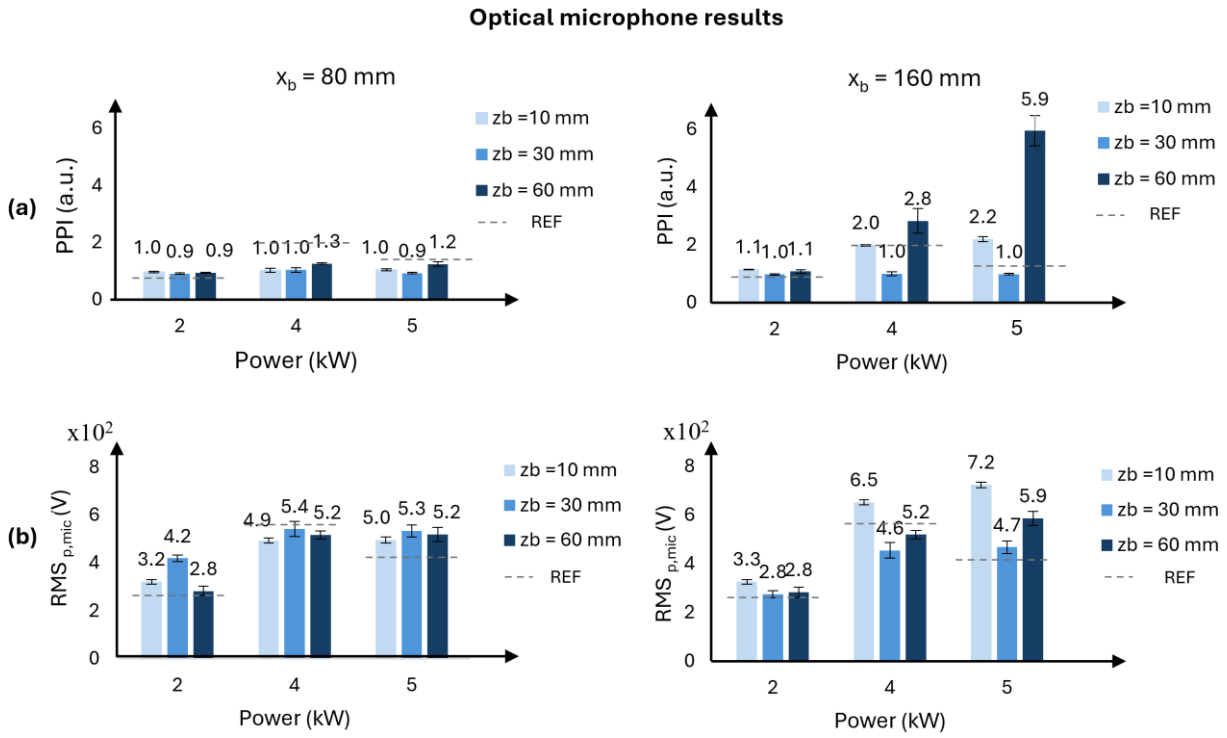

Figure 21: Values derived from the optical microphone's frequency analysis.

When all external noise sources were deactivated, except for shielding gas, the acquired acoustic signal appeared significantly cleaner. As depicted in Figure 9c, the background noise (blue line) still exhibited a higher amplitude than the process-related emissions, regardless of laser power. As previously discussed, a distinct contribution from the process was observed only within the 2–25 kHz range, which also corresponds to the region where background noise had minimal influence (Figure 9d).

To better evaluate process-related acoustic emissions, two indices were introduced: the RMS-based time analysis restricted to 2-25 kHz frequency band ($RMS_{p,mic}$), and the Power Process Index (PPI), which compares the total spectral energy of the process to the background across the whole frequency range. Hence, PPI index provided an effective means of quantifying how much the total spectral content increases when varying process parameters, regardless of background noise.

The results were reported in Figure 21. At x_b = 80 mm in Figure 21a, the PPI indicated that process emissions were negligible and indistinguishable from background noise for all vertical offsets (PPI ≈ 1.0). This suggests poor acoustic coupling or suboptimal microphone alignment at this proximal position.

In contrast, at x_b = 160 mm, the influence of laser power became relevant, and the process signal was more distinct. As shown in Figure 21b, the $RMS_{p,mic}$ increased with laser power, peaking at x_b = 160 mm z_b = 10 mm configuration at 5kW, which corresponds to the highest measured weld depth and minimal plume intensity. Concurrently, PPI rose significantly for the z_b =10 mm to 60 mm configurations. For z_b = 60 mm, a further rise occurred between 4 kW and 5 kW.

However, it is not immediately clear whether this rise stems from an intrinsic enhancement of process-related emissions or simply from a reduction in background noise levels. It was observed that at x_b = 80 mm the process and background spectral energies were nearly identical, confirming a negligible acoustic contribution from the process itself. In contrast, at x_b = 160 mm, the energy within the ROI_p increases substantially, particularly at z_b = 60 mm, indicating that the sensor in this configuration captures a more distinct process-related signature. This might be due to a more energetic plume, greater penetration or

different laser-material interaction. The concurrent rise in PPI reinforces the hypothesis that the measured signal originates from process dynamics rather than random background fluctuations.

Cross-referencing with high-speed video analysis confirmed that this increased energy at x_b = 160 mm, z_b = 60 mm was associated with a more intense plume, consistent with conduction-mode welding behavior. Synthesizing these findings with prior signal analysis, it is evident that the microphone successfully captured plume-related acoustic emissions only when positioned at the further distance (x_b = 160 mm), where the process signal was sufficiently prominent to not be masked by background noise.

6. T11.3 Feature extraction, data labelling, data fusion and augmentation and storage in the database

6.1. Feature extraction, data processing and labelling

For time series data, the general processing pipeline includes: load data, filter data using appropriate noise reduction filter (e.g., low-pass, high-pass, band-pass, Gaussian filters, and median filters), feature extraction (descriptive statistics, frequency content), and storage of the key features in the local database. Descriptive statistics features include mean, standard deviation, skewness, kurtosis, peak amplitude, root mean square, and signal energy. Frequency-domain features are obtained through spectral analysis methods, including Fast Fourier Transform (FFT), power spectral density estimation, and wavelet-based decomposition, enabling identification of characteristic process frequencies, oscillatory behaviour, and transient events.

For image data, the processing pipeline includes: load image, crop image with predefined ROI to reduce computational efforts, convert image in grayscale, enhance contrast to improve detection of features, apply image processing techniques (e.g., edge detection, feature detection, cross correlation), extract features (max beam intensity, seam position, etc.) and storage of the key features in the local database.

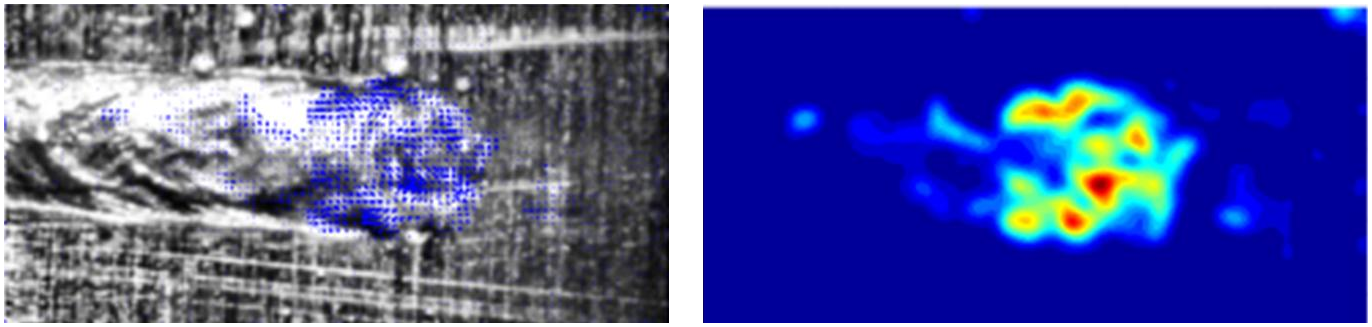

Figure 22: Example of feature extraction (left: video with velocity field; right: velocity map)

To reduce data dimensionality and identify the most relevant process indicators, correlation analysis is initially implemented to down-select significant variables and features. Correlation matrices and feature ranking techniques are used to identify strong relationships between sensor outputs, process parameters, and resulting weld characteristics. Also, tests of hypothesis are coded (for example, ANOVA) to identify the most statistical influential factors and their combined effects on the sensor signals.

The data labelling approach is based on AI-assisted annotation frameworks combining automated pre-labelling, active learning, and human-in-the-loop verification to reduce manual effort while maintaining high-quality datasets. In parallel, semi-supervised learning and synthetic-data generation (see next section as well) approaches are increasingly adopted to minimise the dependency on fully labelled datasets.

6.2. Data fusion and augmentation

The Visualization Toolkit (VTK) format has been selected as the common framework for combining, storing, and integrating synthetic simulation data with experimental sensor data across the project. VTK is an open-source scientific data format and visualisation framework that provides a robust bridge between

high-fidelity numerical simulations (e.g., thermal modelling, and multi-physics simulations) and real-time sensor measurements obtained from manufacturing equipment and monitoring systems. This enables comparative analysis, model validation, and interactive visualisation within a unified digital environment (see previous chapters).

The adoption of VTK also enables interoperability between multiple simulation platforms and data sources, including OpenFOAM, COMSOL Multiphysics, and other numerical modelling environments (e.g., MATLAB, Python) deployed within the project. By standardising the data representation, the framework supports seamless integration across different workflows, allowing process simulations, sensor measurements, and control algorithms to exchange information consistently and efficiently. This common data architecture is particularly important for the Lasers4MaaS digital manufacturing ecosystem, where heterogeneous data streams must be synchronised and interpreted in near real-time.

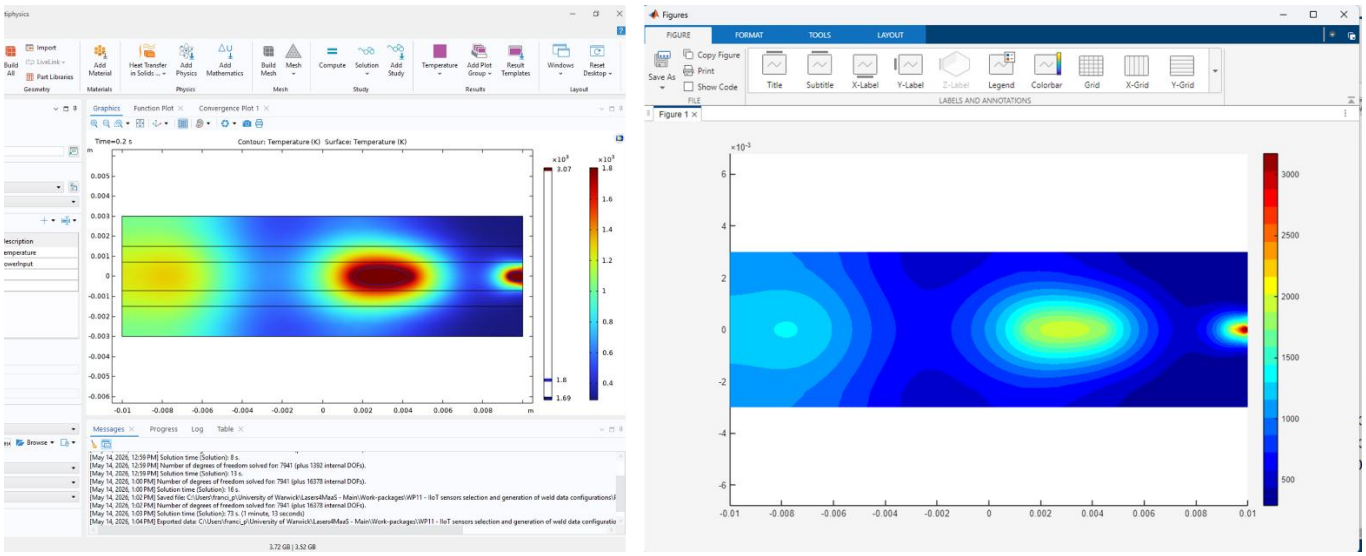

Figure 23: VTK data of a simulated moving laser beam from Comsol (left) to MATLAB (right)

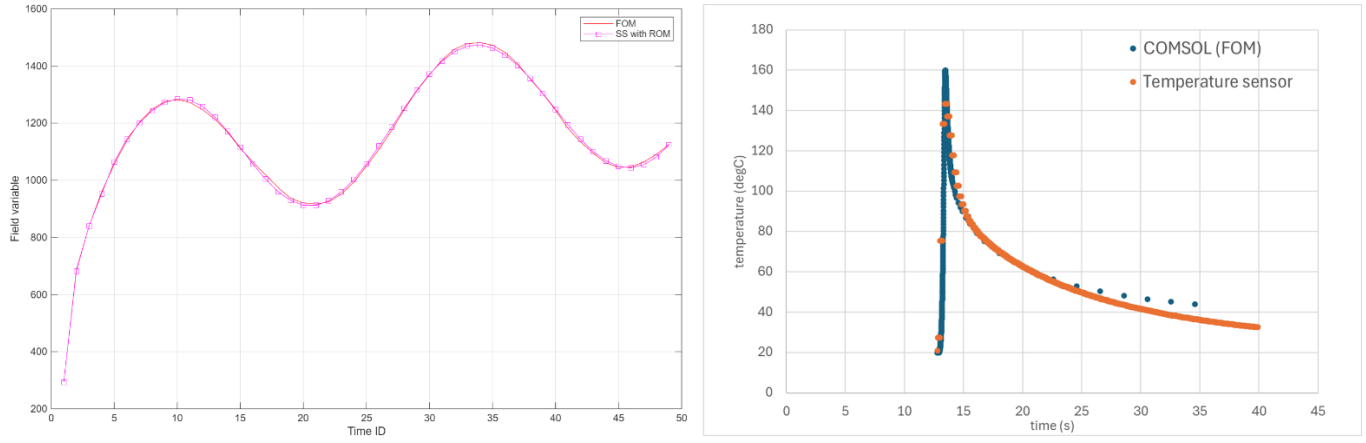

Figure 24: FOM vs ROM (left); interpolation of sensor data to the FOM and ROM models (right)

The data fusion framework supports both spatial and temporal interpolation techniques, enabling direct comparison between experimentally measured sensor data and simulated process outputs. For example, sparse temperature measurements from embedded or surface-mounted sensors can be interpolated onto CFD meshes to assess model accuracy and identify local discrepancies. Similarly, simulation outputs can be sampled at sensor locations to support calibration and validation activities. These capabilities improve confidence in the predictive models while enabling continuous refinement of process parameters and boundary conditions.

In addition to offline analysis, the framework supports real-time data streaming to the Lasers4MaaS platform. Live sensor feeds can be incorporated into the digital representation of the process, allowing updated state estimation, process monitoring, and adaptive control. This functionality is essential for enabling responsive manufacturing systems and digital twins capable of reacting dynamically to changing operating conditions. A key enabler for achieving real-time data transfer and processing within operational time constraints (within seconds) is the ROM capability coordinated in WP10. ROM techniques reduce the computational complexity of high-fidelity numerical simulations while preserving the dominant physical behaviour of the process. These reduced models are deployed across multiple work packages to support rapid process selection, optimisation, prediction, and closed-loop control. By combining ROM outputs with live sensor measurements through the VTK-based data framework, the system can provide fast and computationally efficient predictions suitable for industrial deployment. The standardised data structure includes:

- Spatial coordinates of the data point (x, y, z)
- Temporal information (timestamp)
- Associated field variables and metadata.

The field variables may include quantities such as temperature, pressure, melt pool dimensions, fluid velocity magnitude, turbulence parameters, or concentration fields derived from CFD and multi-physics simulations. For experimental systems, field variables may correspond to sensor outputs including laser power signals, camera-derived features or other process-monitoring signals described in previous chapters. The fusion of simulation and experimental data provides several benefits to the project, including:

- Enhanced validation and calibration of simulation models
- Improved understanding of process physics
- Increased robustness of process monitoring and anomaly detection
- Support for predictive maintenance and adaptive control strategies
- Creation of richer datasets for ML/AI applications
- Improved scalability and portability of digital manufacturing workflows.

Furthermore, the augmentation of experimental data using synthetic simulation data enables the generation of larger and more representative datasets for training data-driven models. The Visualization Toolkit (VTK) format has been selected to combine and integrate synthetic simulation data and sensor data. VTK is an open-source library that acts as a bridge for integrating simulation outputs (such as CFD data) with real-time sensor data, enabling comparative analysis, validation, and visualization. Additionally, this has enabled interoperability across simulation platforms (OpenFOAM, Comsol Multiphysics, etc.) and integration across difference data workflows.

Additional details about the lasers4MaaS consolidated platform database are reported in D5.2 and a summary in the following section.

6.3. Integration with the Lasers4MaaS platform and storage into the database

Apart from camera images, all sensor data is transmitted to the Lasers4MaaS platform in the cloud and stored in the platform's database. This enables remote monitoring of the welding processes, as well as the prediction of required maintenance through anomaly detection.

From the acquisition system on the shop floor, the data is transferred to the Lasers4MaaS platform's cloud-hosted database in two steps:

- A Python application running on the local workstation, called the *Monitoring Data Uploader*, regularly sends the latest sensor data to a message queue (specifically, a NATS[1] server) running in

[1] https://nats.io/

the cloud. Each welding station is represented as a separate queue ("subject" in NATS' terminology), making it possible for the platform to determine which station the data originates from.

- Within the cloud platform, a service subscribes to the message queues and writes the sensor data into the platform database.

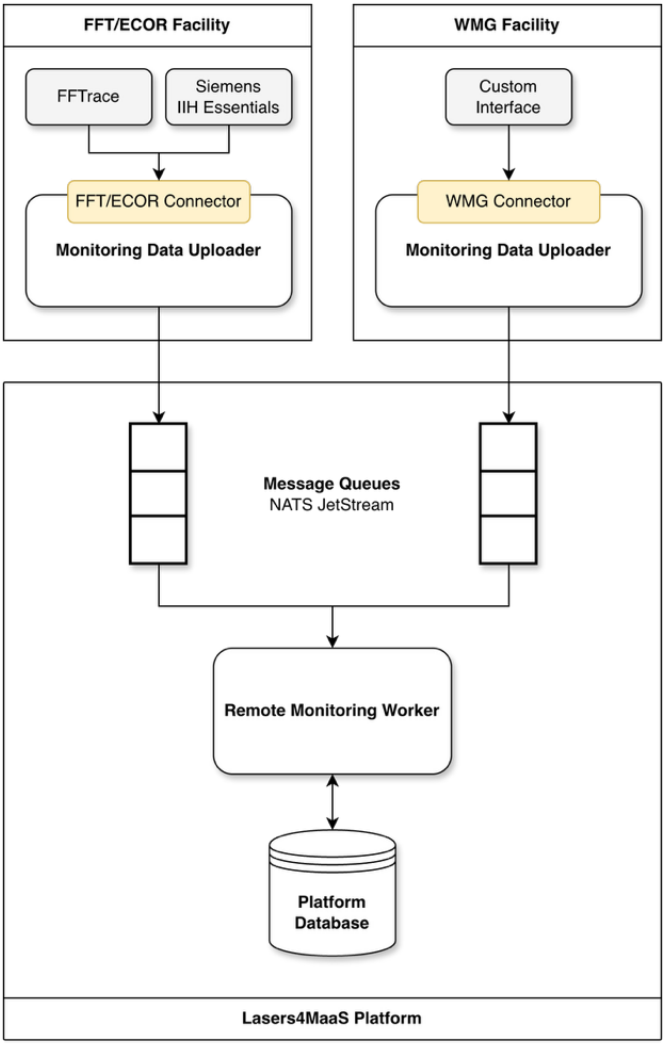

Figure 25: Data flow to the Lasers4MaaS platform

The intermediate message queue decouples the local application from the database, and also makes it possible for the platform to batch and/or throttle writes to the database to limit the load on it.

Each Monitoring Data Uploader installation has unique NATS credentials, with permissions limited to writing to the message queues corresponding to the facility's welding stations. Furthermore, the application is deployed and run as an OCI (Docker) container, limiting its access to the host system. These measures minimize the application's attack surface.

To abstract away the differences between the FFT/ECOR and WMG facility setups, the Monitoring Data Uploader application has the notion of *connectors*, which encapsulate the process of retrieving the sensor data and translating it to the JSON format expected by the platform. For instance, the connector for FFT/ECOR fetches data from a Siemens IIH Essentials[2] instance, while the one for WMG retrieves them through a custom-built interface. This design allows the application to be easily adapted to new deployment

[2] https://www.siemens.com/en-us/products/industrial-edge/iih-essentials/

scenarios as the required code changes are limited to developing a new connector or extending an existing one.

7. Summary observations

Each sensing approach was assessed in terms of feasibility, integration capability, signal quality, and suitability for monitoring during laser welding operations, mechanical and optical constraints and integration with the IIoT infrastructure. The colour coding adopted in the table provides an overview of the final assessment of each sensor technology, where green indicates a feasible and successful implementation, amber identifies technologies with potential applicability but limited operational scope, and red denotes approaches considered unfeasible under the investigated process conditions. Based on these findings, the selected sensors represent the most promising solutions to be carried forward into the next stages of the project development.

Table 2: Summary of sensors for product and process monitoring.

What	Sensor	Comments
Gas flows	SDR32DGXFRKG/US-100	Industrial standard
Energy consumption	Siemens 3VA9987-0TA20 SD9500	Industrial standard
Scanner laser output	Data acquired from control card	Industrial standard
Laser source output	Ophir PD300	This is a major innovation in the project
Photodiode	LWM Precitec	Indirect measurement (process light, laser BR, temperature). The sensor is industrial standard but the integration with the CIVAN DBS is the first time
Alignment co-axial camera	Image Source DMK 33UX287	Industrial standard, but coordination with the IIoT infrastructure is the first time
Beam shape camera	IDS GV-5880CP-M-GL	Industrial standard, but coordination with the IIoT infrastructure is the first time
Acoustic	Xarion Eta 250 ultra	Indirect measurement (Airborne sounds/ultrasound)
Depth of keyhole monitoring	OCT	Failed to measure keyhole/capillary depth due to attenuation of the OCT beam occurred through the optical path/scanner mirrors

Regarding optical emissions monitoring, a co-axial photodiode sensor was investigated to capture indirect process signatures associated with the welding operation. The photodiode measurements provide information related to process light intensity, laser back-reflection and thermal emissions from the melt pool region. Although the signal does not directly measure weld quality metrics, it offers valuable high-speed information correlated with process stability and keyhole behaviour.

For seam surface monitoring, both co-axial and off-axial camera configurations were evaluated. The co-axial camera arrangement was primarily used for alignment purposes, enabling accurate tracking of the tool centre point (TCP) position relative to the weld path. In contrast, the off-axial camera configuration was implemented for direct observation of the weld seam geometry and surface condition. This setup enabled the identification of seam discontinuities and the measurement of top seam width, providing important information regarding weld consistency and defect formation.

The OCT system was ultimately found to be unsuitable for implementation in the current scanner configuration because the operating wavelength of the OCT source (~850 nm) coincided with a low transmission region of the scanner mirrors. As a result, significant attenuation of the OCT beam occurred through the optical path, preventing reliable acquisition of keyhole depth measurements.

Acoustic monitoring was also explored using an optical microphone based on a Fabry–Pérot interferometer. This sensor enables indirect measurement of airborne acoustic emissions and ultrasonic process signatures generated during laser welding. The acquired signals can potentially be correlated with process instabilities, spatter formation, and keyhole dynamics, although further work is required to fully establish robust relationships between the acoustic response and weld quality metrics. Main limitation is the sensitivity to cross-jet noise.

A key innovation asset is the laser analogue power monitoring system, integrated with the sensors described in this deliverable. This will enable the possibility to monitor the laser process, observe drift over time, and rapid resolutions of process and machine failures. The data streams will be coordinated by the Lasers4MaaS platform, and enhanced by the related services.

On the data interoperability, the VTK format has been selected as main data format to transfer data from simulation and integrate with sensor data. More details are also presented in deliverable D9.1.

8. Contribution to project KPIs and expected outcomes

The outputs of D11.1 primarily contribute to the CONNECT KPIs, while also supporting the CONTROL, IMPROVE, and COMPLY objectives of the project.

From the CONNECT perspective, the developed IIoT-enabled process and machine-related sensing infrastructure enables real-time data streaming from local acquisition systems to the Lasers4MaaS platform, as further detailed in D5.1 and D5.2. *Standardised data formats*, including JSON and VTK, have been adopted with field naming aligned to the Welding Process Analytics Database architecture defined in D5.2. The implemented sensing and data infrastructure directly supports *predictive maintenance and remote monitoring* functionalities, enabling remote diagnosis and resolution of product defects and machine failures. For example, continuous monitoring of laser power output enables verification of laser operation within specification, detection of degradation or abnormal behaviour, support for closed-loop power regulation, improved process repeatability, and preventive maintenance. Similarly, beam shape image monitoring enables trend analysis of beam shape quality over time.

From the CONTROL and IMPROVE perspectives, the work developed in D11.1 enables the implementation of the closed-loop control architecture described in D9.1. The integration of sensor systems with ROM and *AI-based controllers supports real-time adaptive process control*, contributing to reduced defect rates and minimised manual rework operations. In addition, the capability to monitor process energy consumption contributes directly to the COMPLY objectives by supporting assessment and reduction of operational energy usage within laser manufacturing processes.

9. Impact and exploitation potentials

CIVAN: The laser analogue power monitoring system is a major exploitation asset which, once fully validated (WP15 and WP16) will be considered for further exploitation. Additionally, the project has integrated for the first time a photodiode sensor with the DBS laser for weld quality monitoring. The possibility to monitor and process the laser power output has significant potential for verifying that the laser operates within specification, detect degradation or abnormal laser behavior, enable closed-loop power regulation, improve process repeatability and product quality, support machine diagnostics and preventive maintenance. Similarly, the monitoring of beam shape images will enable trend graph of beam shape over time, which is essential for quality assurance.

FFT: From FFT's perspective, the integration and standardized acquisition of diverse sensors and machine data enhance the available machine interfaces and creates a basis for further digital services. Harmonized interfaces ensure that the developed solutions remain application-neutral, enabling transferability to other use cases and supporting the realization of flexible, reconfigurable production systems. By systematically collecting and structuring process, component, and system data, advanced monitoring and analytics methods could be used. In particular, the subsequent use of this data enables improved transparency regarding machine status, component quality, and process stability. This increases operational efficiency and quality assurance but also ensures exploitation potential such as predictive maintenance, process optimization, and data-driven services and is strengthening FFT's position in the field of intelligent production systems.

FUTURICE: FUTURICE's exploitation strategy focuses on the commercialization of the Lasers4MaaS digital backbone, positioning the company as a provider of a "Sovereign Industrial Coordination System" that enables manufacturing servitisation. This strategy is built on the transition from selling stationary hardware to orchestrating dynamically routed, hardware-agnostic manufacturing capacity. The core exploitable asset is the modular, microservices-based MaaS Digital Platform, which decouples process intelligence from physical execution to act as a "Laser Operating System". A critical component of this platform is the Monitoring Data Uploader and its modular "connector" architecture, which allows for the rapid and secure integration of heterogeneous shop-floor sensor data into cloud-hosted databases. By deploying these as containerized OCI (Docker) images with unique credentials, FUTURICE ensures a minimized attack surface, effectively protecting a manufacturer's sensitive process intellectual property while maintaining data sovereignty. The platform further leverages high-value digital services such as Generative AI-based assistance to surface institutional knowledge and real-time visualization dashboards. These tools synchronize high-fidelity sensor streams with ROMs to facilitate the "Digital Handshake"—a process that validates manufacturing recipes on digital twins in near real-time. This capability is essential for overcoming the "Physicality Gap" allowing digital definitions to be transferred across different machines regardless of hardware variance. Strategically, FUTURICE exploits the shift toward "system-versus-system" competition by providing the necessary Meso-level trust framework that allows SMEs and large manufacturers to collaborate in decentralized production networks. This coordination logic enables Industrial Grid Balancing, where production loads are dynamically shifted to regions with high renewable energy availability, while simultaneously automating regulatory compliance for upcoming initiatives like the Digital Product Passport (DPP).

WMG: we are motivated by the need to develop laser welding processes using long-focal length configurations with integrated CBC-OPA, particularly suitable for rapidly repositioning the beam to follow complex seam contours over a large field of view. In conventional welding heads, the airblade is integrated into the mechanical system, positioned close to the processing zone and moves together with the laser beam and the welding heads. However, this approach becomes impractical for long-focal length setups (>1 m), where the laser beam interacts with an extended plume volume. This capability is particularly relevant for laser welding in high-volume manufacturing domains, including automotive battery cooler production, demanding high-speed scanning solutions over large areas to meet cycle time. We have demonstrated for the first time the impact of airblade positioning and laser power on weld quality. This is achieved through synchronized acquisition of optical microphone, photodiode, and high-speed imaging data. The resulting quantitative correlations between airblade position and weld quality are expected to inform the design of advanced long–focal length laser welding systems with integrated CBC-OPA, clamping units, shielding gas delivery and airblade functionality. The scientific contribution (peer-reviewed) is currently under review under Optics and Laser Tech Journal. Additionally, the sensor fusion approach presented in this deliverable represents a very good opportunity to enhance WMG's research opportunities in process control using ML/AI, real-time decision-making and process optimisation, and intelligent manufacturing systems.